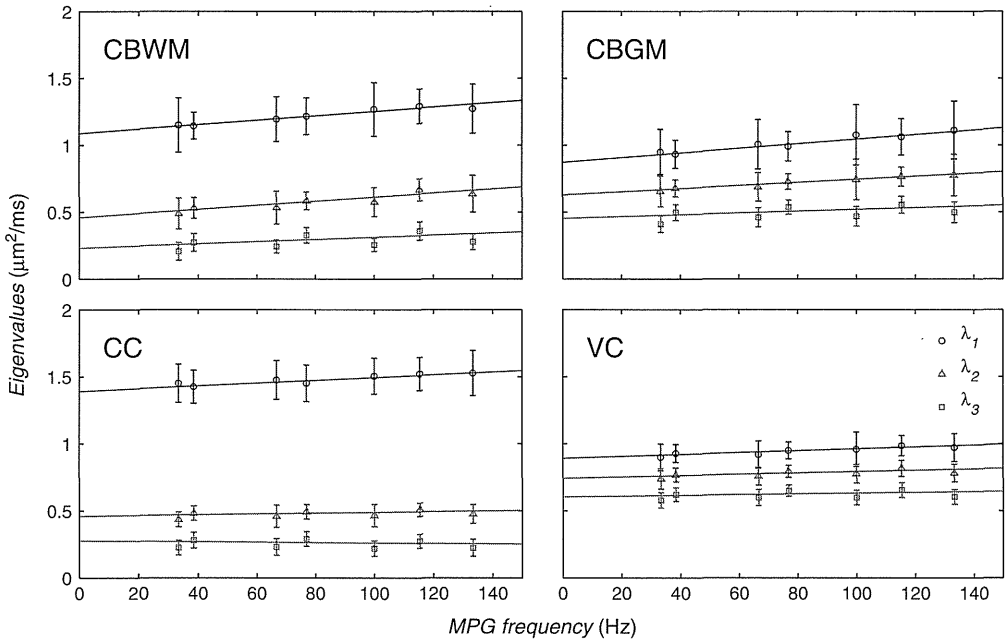

Fig. 6. The EVs of the ADT plotted against MPG frequency for all four ROIs. The error bars represent the standard deviation of the EVs across animals and experiments at the same frequency. The solid lines are straight line fits to the data, with the estimates and uncertainty of the slopes shown in Fig. 7.

the CC as minor increases to the MD and FA corresponded to a strong increase in the first EV, but only minor or no changes to the two smaller EVs. At the same time, there was no clear indication that the orientation of the principal eigenvectors varied systematically with the applied frequency for any of the ROIs.

Comparison with previous OGSE DTI of brain tissue

Recent OGSE DTI observations made by Aggarwal et al. (2012) on ex vivo mouse brains over the range 50–150 Hz also found that the MD (denoted by ADC in that study), FA and EVs varied linearly with MPG frequency. They also found no evidence that the primary direction of the ADT was altered with frequency. The most dramatic dependences on frequency were observed in the granule cell layer of the dentate gyrus, the pyramidal cell layer of the hippocampus, and the cerebellar granule cell layer (CBGr). By performing pixelwise linear fits with respect to MPG frequency, it was demonstrated that maps of the slope provide a novel tissue contrast in diffusion-weighted MRI of mouse brain. While it was not clear what the mechanism driving the contrast change is, comparison to immunohistochemical staining found that regions with enhanced MD largely correspond to areas with densely-packed neurons having relatively large nuclei. From this result and simulations performed with a simplified model of cell structure (Xu et al., 2009), it was suggested

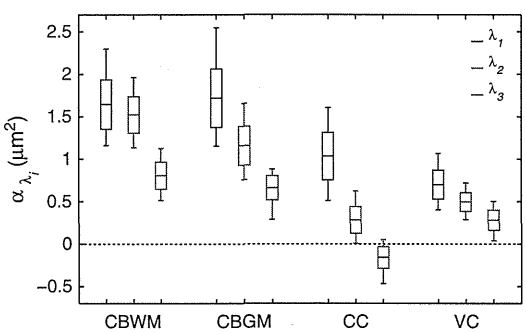

Fig. 7. Box-whisker plots of the α_{λ_i} estimated from straight-line fits to the EVs of the ADT with MPG frequency for all ROIs. The boxes represent the standard deviation of the estimates and the thinner bars are the 95% confidence intervals.

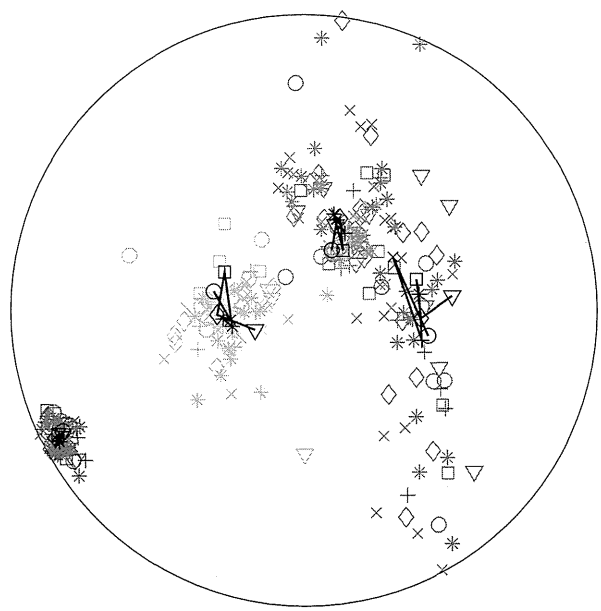

Fig. 8. Lambert equal-area projection of the principal eigenvectors of all ROIs onto the tangent plane passing through the point (0.48, 0.48, 0.73) on a unit sphere. Each point represents where the tip of a particular eigenvector lies on the sphere. The region inside the black circle is an area-preserving map of the upper hemisphere onto the plane. Points have been plotted using the same colour scheme originally used in Fig. 2. The eigenvectors from each ROI have been grouped according to MPG frequency with the following correspondences between the symbols and frequency: ○, 33.33 Hz; ×, 38.5 Hz; +, 66.6 Hz; ✳, 76.9 Hz; □, 100 Hz; ◇, 115.4 Hz; ▽, 133.3 Hz. The black symbols and lines illustrate the progression of the mean direction with frequency for each ROI. The points are joined in the order of increasing frequency, but there does not appear to be any simple deterministic pattern to the arrangements. The results of a hypothesis test evaluating the consistency of the mean directions with frequency are presented in Table 2.

Table 2
P-values from hypothesis tests evaluating the consistency of the principal eigenvector orientation with MPG frequency. The hypothesis tests for the CBWM, CBGM and CC were based on a bipolar Watson distribution, and that for the VC was based on a girdle-like Watson distribution (Mardia and Jupp, 2000).

ROI	CBWM	CBGM	CC	VC
P	0.31	0.056	0.19	0.057

that α_{MD} may be correlated with the nuclear volume fractions of the cells in those regions.

As there is a clear correspondence between the morphology of the rat and mouse brains, a similar pixelwise linear fit to the data from individual animals was performed to investigate whether changes to the MD can be discerned across the area imaged in the present research. The example presented in Fig. 9 shows no obvious changes in the visual cortex, corpus callosum or other parts of the caudal cerebrum, but there is a clear elevation of α_{MD} across the cerebellum. Enhanced pixels have α_{MD}s in the range 2–4 μm^2, which is ~2–3 times larger than the values found for the CBWM and CBGM ROIs (but similar to the value of 3.6 μm^2 estimated from Fig. 4c of Aggarwal et al. (2012) for the CBGr in ex vivo mouse cerebellum; see Supplementary Table 1). Unfortunately, the contrast is not sharp enough and the resolution too coarse to unequivocally attribute the enhancement to a specific tissue type by eye. Moreover, the histograms in Fig. 9b demonstrate that there was no exclusive correspondence between pixels with elevated α_{MD} and one or other of the cerebellar ROIs. If the source of this in vivo enhancement is the same as the ex vivo CBGr enhancement found by Aggarwal et al. (2012), then the granular cells may have influenced both the CBWM and CBGM results. Fig. 10 presents sagittal histological sections from an 8 week old rat. As well as the CBGr, the grey region in the cerebellum consists of two other cellular layers with distinct structural characteristics: a single layer of Purkinje cells and a superficial molecular layer. The Purkinje layer is probably too thin to have a significant effect on the diffusion-weighted signal so that the granular and molecular layers most likely dominate any signal changes. Pixels selected for the CBGM ROI were located in the prepyramidal and secondary fissures of the cerebellum at least one pixel away from any pixels considered to be white matter, but there was no way to differentiate between the CBGr and molecular layers. At the same time, the criteria for CBWM pixels was that they had FAs of 0.5–0.8 and were clearly located in the regions commonly designated as white matter on T_2-weighted images. However, in the sagittal orientation the white matter branches in the lobules of adult rat cerebellum are at most 300–400 μm thick (Fig. 10), which is comparable to the spatial resolution of the MR images. It is therefore likely that pixels in both the CBWM and CBGM ROIs contained contributions from the CBGr, and this may explain why the cerebellar ROIs had similar α_{MD}s.

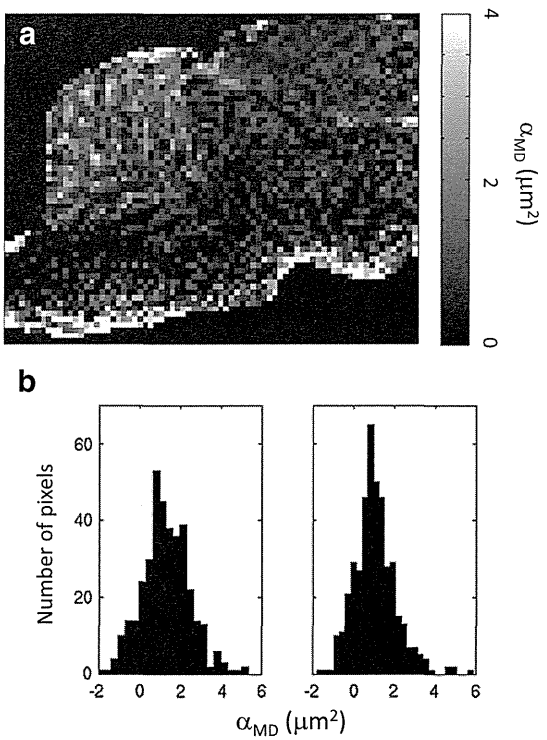

Fig. 9. (a) Map of α_{MD} for the same rat as shown in Fig. 2. Note the enhanced values in the cerebellum. (b) The α_{MD}s of all pixels in the CBWM and CBGM ROIs of all animals have been placed in histograms to demonstrate that pixels with elevated values were not exclusive to either ROI.

Fig. 10 also contains images of the tissue in the corpus callosum and visual cortex. It is immediately evident that the distribution of nuclei in both of these areas is quite sparse in comparison to the CBGr, and the nuclei in the VC are much larger in diameter than those in any of the other ROIs (Table 3). The results of conventional PGSE or PGStE DTI have long been used to infer the geometry of these tissues. For example, it has been conjectured from conventional DTI that tissue in the CC has an elongated structure that is predominantly oriented along the principal axis of the ADT. Histology of the corpus callosum is consistent with this picture. The OGSE DTI results also do not contradict the presumption of an elongated geometry and in fact hint that more subtle structural information may be available. This assertion is supported by a recent application of the OGSE sequence to ex vivo rat spinal cord (Xu et al., 2012). With the MPG applied perpendicular to the primary fibre direction, it was found that the rate of change of the apparent diffusion coefficient (ADC) with frequency is linearly correlated with the mean axon diameter in different white matter tracts. It is possible that high spatial resolution OGSE DTI might be used as a noninvasive method to measure the mean axon diameter of fibre bundles in the CC and other white matter tissues.

In a similar way, conventional DTI implies that tissue in the VC is fairly homogeneous because the EVs have similar magnitudes and the FA is relatively low. However, with reference to the water sample, which is homogeneous and where all of the EVs and the FA accordingly show no dependence on frequency (Fig. 1), the OGSE DTI results correctly indicate that the tissue must in fact be inhomogeneous. It is difficult to identify from the type of stain used for Fig. 10 what part of the tissue may be directly responsible for the changes to the ADT, but it is well known that the visual cortex of both rodents and humans has a stratified cellular structure and a large number of nerve fibres running radially towards the cortical surface (e.g. Demyanenko et al., 2004; Leuze et al., 2012). The larger volume of cortical nuclei is another factor that may contribute.

As already noted in the Introduction, the only other complete application of OGSE to DTI was a small study performed on the cerebrum of an ex vivo monkey brain (Xu et al., 2010). Unfortunately, the results have not yet been published in full, but it is known that the FA was found to vary approximately linearly over the range 50–300 Hz. For a white matter ROI the FA decreased at a rate of about 0.8 kHz^{-1}, while the FA was relatively unaffected by MPG frequency for a grey matter ROI.

Finally, even though the full ADT was not measured, Does et al. (2003) did apply the OGSE sequence to estimate the MD of in vivo rat brain over the frequency range 38.5–500 Hz. The MD was found to increase substantially with increasing frequency, however, a solid comparison with the present data is hindered by the fact that the only measurements within the range 33.3–133.3 Hz were at 38.5 and 115.4 Hz. Nevertheless, if it is assumed that the MD is approximately linear in that range, a crude estimate from Fig. 8 of (Does et al., 2003) finds that the slope in normal cortical grey matter is around

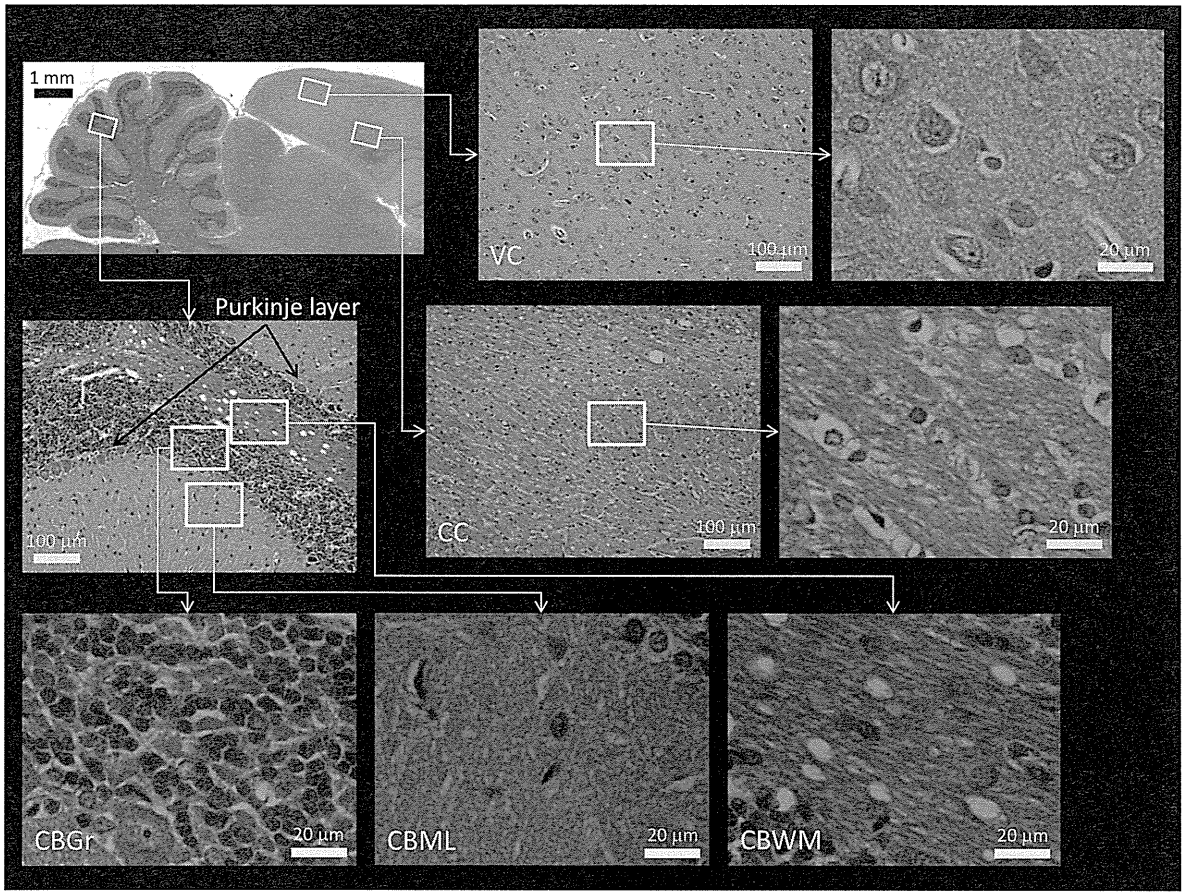

Fig. 10. Histology sections from an 8 week old rat in the same orientation as the imaging was performed. The tissue has been stained with haematoxylin and eosin, which stains cell nuclei blue or purple and the cytoplasm, connective tissue and other extracellular substances various shades of pink or red. The yellow rectangles on the figure in the upper left corner show the locations of the higher magnification images pointed to by the arrows, and this pattern is repeated for the rectangles in the next level of images. A scale bar is also shown on each image. Each of the higher magnification images zooms in on an area within the ROIs studied in the manuscript. Note that, rather than just CBWM and CBGM images, the cerebellum has been classified into three tissue categories: the CBWM, cerebellar granule cell layer (CBGr) and cerebellar molecular layer (CBML).

$0.36\mu m^2$, which is compatible with the MD estimate found here for the VC ROI.

On the changes to the MD and FA with frequency

From the results in Figs. 6 and 7 it is immediately clear why the MD behaves as it does in Figs. 3 and 4a. Denoting the ith EV at frequency f by λ_i, over the range of frequencies used it was found that

$$\lambda_i \simeq \alpha_{\lambda_i} f + \beta_{\lambda_i}, \tag{1}$$

which means that $dMD/df \simeq \alpha_{\lambda_1} + \alpha_{\lambda_2} + \alpha_{\lambda_3}$. It follows that the MDs of the CBWM, CBGM and VC increase strongly with MPG frequency because all of the EVs do, while the increase in MD of the CC is less dramatic because only the largest EV increases substantially with frequency.

Table 3
Characteristics of the nuclei in the highest magnification images of Fig. 10.

Tissue	Nuclear diameter (μm)	# Nuclei	% of total area
CBWM	8–10	16	7–12
CBGr	4–6	205	23–52
CBML	6–8	10	3–5
VC	12–14	16	16–23
CC	4–6	22	2–6

An explanation for the behaviour of the FA (Figs. 4b and 5) is a little more complicated. First note that even though the FA is defined as a nonlinear function of all three EVs ($\lambda_1 \geq \lambda_2 \geq \lambda_3 \geq 0$) (Basser and Pierpaoli, 1996), by making the change of variables $(\mu_1,\mu_2) = (\lambda_2/\lambda_1, \lambda_3/\lambda_2)$ it can be rewritten as a function of only two independent variables

$$FA(\mu_1,\mu_2) = \sqrt{\frac{(1-\mu_1)^2 + (1-\mu_1\mu_2)^2 + \mu_1^2(1-\mu_2)^2}{2[1+\mu_1^2(1+\mu_2^2)]}} \tag{2}$$

with domain $[0,1]\times[0,1]$. The advantage of this form is that the reduced number and finite range of the independent variables allows the changes to the FA and EVs to be simultaneously visualised on a contour plot like that shown in Fig. 11. At any point $\boldsymbol{\mu}$ on the plot

$$\frac{dFA}{df} = \partial_{\mu_1} FA\left[\frac{d\mu_1}{df} + \kappa\frac{d\mu_2}{df}\right], \tag{3}$$

where $\kappa = \partial_{\mu_2} FA/\partial_{\mu_1} FA$ has been defined. A quick glance at the figure establishes that $\partial_{\mu_1} FA < 0$ and $\partial_{\mu_2} FA \leq 0$ throughout the domain, and therefore it is always true that $\kappa \geq 0$. After using Eq. (1), it is also easy to see that $d\mu_j/df \simeq \left(\alpha_{\lambda_{j+1}}\lambda_j - \alpha_{\lambda_j}\lambda_{j+1}\right)/\lambda_j^2$ is positive or negative depending on whether $\alpha_{\lambda_{j+1}}/\alpha_{\lambda_j}$ is greater or less, respectively, than λ_{j+1}/λ_j $(=\mu_j)$. For example, for the CBWM ROI the 1st and 2nd EVs increase strongly with frequency at about the same rate (Fig. 7), but because the value of λ_2 is substantially less than λ_1 (Fig. 6), an

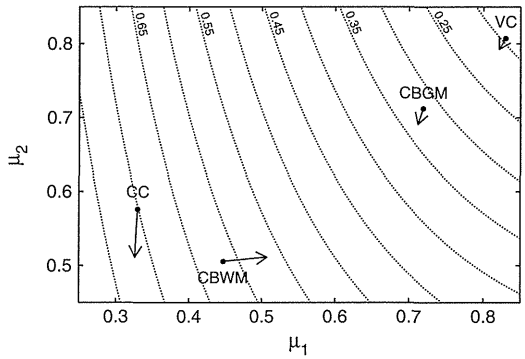

Fig. 11. Contour plot of $FA(\mu_1,\mu_2)$ as defined in Eq. (2). The horizontal and vertical axes correspond to μ_1 and μ_2, respectively, and the dotted contours represent lines of constant FA in steps of 0.05. Although the full domain of μ_1 and μ_2 is not shown in the figure, note that the point $\mu_1=\mu_2=1$ corresponds to $FA=0$ and from there the FA increases as either μ_1 or μ_2 decreases. Note also that the FA is always equal to 1 whenever $\mu_1=0$, and there are no local maxima, minima or saddle points within the domain. The positions of the closed circles correspond to the estimates of μ_1 and μ_2 at the lowest applied MPG frequency (33.3 Hz) for each of the in vivo ROIs. The solid line extending from each circle traces out the changes to the EVs and FA with increasing frequency before terminating with an arrowhead as the highest applied frequency (133.3 Hz) is reached. For the purposes of simplifying the figure, the uncertainty of the estimates has not been plotted.

increase in μ_1 with f results. Finally, knowing how these factors vary with frequency it can be understood from the figure that the FA decreases for the CBWM because both μ_1 and μ_2 increase with frequency. Similarly, the FA increases for the CBGM, CC and VC because μ_1 and μ_2 both decrease with frequency, although it should be remembered that the uncertainty analysis indicates that the changes to the FA are not significant or only minor for these ROIs (Figs. 4 and 5). In general, the FA may either increase or decrease depending on the size of the EVs relative to each other and also on the rates of change of the EVs with frequency.

Extracting quantitative morphological information: restricted diffusion and asymptotic diffusion-time behaviour

The results of this study demonstrate that OGSE DTI provides a qualitative advantage over conventional DTI because changes to the ADT have been observed in in vivo experiments. However, an important question remaining for OGSE DTI studies is how can this additional information be used to quantify the structure or condition of brain tissue? A potential means to extract quantitative information is to interpret the data within the mathematical framework developed for restricted diffusion.

The study of restricted diffusion with NMR has a long history stretching from the 1960s until the present (Grebenkov, 2007). In that time many theoretical studies have addressed the *forward problem* of calculating how a known geometry influences molecular diffusion and the corresponding signal attenuation (e.g. Tanner, 1978; Sukstanskii et al., 2004). In the theory, the physical problem of calculating the signal can be reduced to the mathematical problem of analysing the spectral properties of the Laplacian in the given geometry. As the eigenmodes are directly related to the shape of the confining medium, there is a great deal of information about the geometry encoded in the signal. It is therefore the *inverse problem* of what and how morphological information can be inferred from the observed signal that is more relevant to practical applications. One way to address this problem is to solve the forward problem for a model system and then fit the observed signal to the model to quantify the parameters defining the geometry. Although this strategy is used to some degree for successful fibre-tracking in white matter (e.g. CHARMED Assaf et al., 2004; AxCaliber Assaf et al., 2008) and estimating the dimensions of packed cell preparations (e.g. Xu et al., 2011), it has the obvious weakness of requiring some prior knowledge of the medium's geometry and the way the diffusing molecules interact with the microstructure. Moreover, it may be very difficult to describe the geometry of a complex medium with a manageable set of length parameters and some essential features of the system may be missing. In disordered media it is likely that the microstructure involves a wide range of length scales so that even the forward problem becomes formidable. It would be beneficial if a model-independent approach were available to characterise media with complicated internal architectures.

Perhaps the most extensive application of the concepts of restricted diffusion is the study of porous media (Sen, 2004). In materials of this type, diffusion-time dependent changes to the signal are often interpreted in terms of the asymptotic short- and long-time behaviour of the ADC. To be specific, in the limit of short diffusion-time (denoted by τ) it has been shown that the ADC approaches the free-diffusion value as $\sqrt{\tau}$, with the constant of proportionality related to the surface-to-pore-volume ratio of the medium (Mitra et al., 1992, 1993). At long diffusion-times the ADC is said to reach a constant value that is equal to the free-diffusion coefficient reduced by a geometrical factor called the tortuosity of the medium (Latour et al., 1994, 1995). Furthermore, this limiting value is approached as $1/\tau$, but, unlike the case for short τ, the geometrical meaning of the constant of proportionality is not universal as it depends on the details of the system at hand (Sen, 2003; de Swiet and Sen, 1996). Neither of these limits provides specific details of the pore geometry, but the coefficients estimated from the asymptotic τ behaviour of the data can be used to characterise the medium in a geometrical sense.

While the behaviour of water in living tissue is more complicated than that in an inanimate porous medium, it is thought that many of the concepts of restricted diffusion can also be applied to biological systems (Helmer et al., 1995; Sen, 2003). The strongest evidence for restriction effects in vivo is nonexponential signal attenuation at high b-values (e.g. Assaf and Cohen, 1998; Pfeuffer et al., 1999) and modulation of image contrast with MPG orientation (e.g. Moseley et al., 1990; Doran et al., 1990). Other studies have argued that differences in the signal attenuation for the same high b-value and a range of very long diffusion-times, indicate water exchange between spatial compartments separated by barriers that hinder molecular motion (e.g. Pfeuffer et al., 1999; Clark and Le Bihan, 2000; Meier et al., 2003). In fact, most of the changes needed to adapt the theory of restricted diffusion to biological investigations can be achieved by altering the boundary conditions to accommodate membrane permeability. One model following this approach found that even after doing so, the short-time behaviour of the ADC is unaffected from the case for porous media (Sen, 2003). That is, inclusion of the permeability only alters the coefficients of terms with linear or higher order dependence on τ. In contrast, it has been suggested that the ADC asymptotically approaches its long-time limit as $1/\sqrt{\tau}$ rather than $1/\tau$ when membrane permeability is accounted for (Sen, 2004). In this case the expansion coefficient depends on the permeability as well as pure geometry effects (Latour et al., 1994).

One way that the results presented in this manuscript can be considered in the context of restricted diffusion is to make use of the improvised effective diffusion-time (Does et al., 2003; Gross and Kosfeld, 1969; Parsons et al., 2003). Even if the effective diffusion-time is only valid over a limited range of frequencies (Novikov and Kiselev, 2011), it is assumed that it can be used in this case because the spectrum of applied frequencies (33.3–133.3 Hz) is relatively narrow. Replacing f by $1/4\tau$ in Eq. (1), it is immediately apparent that those EVs of the ADT having a significant dependence on MPG frequency correspondingly have a $1/\tau$ dependence on diffusion-time, fulfilling the hopes for the OGSE sequence expressed near the end of the Introduction. To illustrate the point further, the EVs of the CBWM ROI (normalised by the diffusion coefficient of free water at 37°C (Goodman et al., 2005)) have been replotted as a function of τ in Fig. 12. Also, after inserting the estimates of α_{λ_i} and β_{λ_i} for the

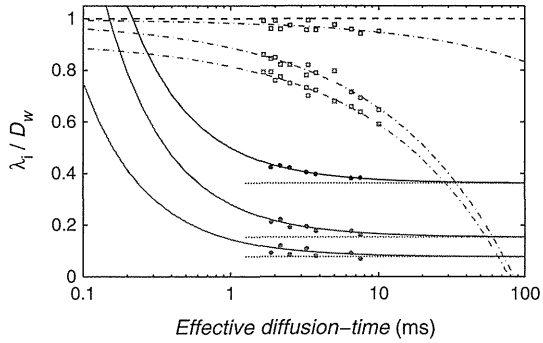

Fig. 12. The EVs of the CBWM ROI (closed circles) normalised by the diffusion coefficient of free water at 37 °C ($D_w \approx 3\mu m^2/ms$) have been plotted against the effective diffusion-time. The solid lines are fits to the data with Eq. (1) and $f = 1/4\tau$, while the horizontal dotted lines represent the predicted asymptotic limit as τ approaches ∞. Similar behaviour was also found for the other rat ROIs. These curves suggest that the rat data was acquired near to the long diffusion-time limit. For comparison, the EVs of the asparagus data (open squares) normalised by the diffusion coefficient of water at 22 °C ($D_w \approx 2\mu m^2/ms$) are also plotted. The dashed lines are reasonable fits to the data as a linear function of $\sqrt{\tau}$, and suggest that the asparagus data might have been acquired in the short diffusion-time limit for this sample.

CBWM EVs into Eq. (1), curves extrapolating the behaviour of the EVs to the range 0.1–100 ms have been drawn on the figure. For diffusion-times above 10–20 ms the figure predicts that the EVs approach a constant value, while for the range below 1 ms the curves forecast that the EVs increase towards the free-diffusion limit as the diffusion-time decreases. Although not shown, similar trends were also found for the other rat ROIs. These results suggest that the rat data was acquired near to the long diffusion-time limit. For comparison, the asparagus EVs (normalised by the diffusion coefficient of water at 22 °C) have also been replotted as a function of τ on Fig. 12. It is evident that the asparagus data does not behave as either $1/\tau$ or $1/\sqrt{\tau}$. However, after noting that the largest asparagus EV is very close to the free-diffusion limit, a fit to $\sqrt{\tau}$ was performed for each EV. From inspection the fit seems to be in good agreement with the data over the range of available diffusion-times. It is therefore possible to deduce that the asparagus data is compatible with the short diffusion-time limit.

Even though Fig. 12 suggests that the rat and asparagus data may be interpreted in the long and short diffusion-time limits, respectively, it does not automatically follow that the parameters estimated from the fits with respect to τ correspond to the coefficients associated with the asymptotic behaviour of the ADC discussed above. The short and long diffusion-time asymptotics predicted by the theory were constructed under the assumption of statistical isotropy at macroscopic length scales, for which case the diffusion behaviour can be described by a scalar function of τ. To the best of the authors' knowledge, an extension of the asymptotic theory to media with macroscopic anisotropy has not been previously considered in the restricted diffusion literature. Without providing a rigorous derivation, it is possible to consider that issue here. First of all, the short-time limit of the ADT must be the same as it is for the scalar case: the diffusion coefficient of free water. However, rather than the ADT collapsing to a scalar before reaching the limit, it seems more likely that each EV of the ADT independently approaches the limit as $\sqrt{\tau}$ at its own rate. Therefore, a possible generalisation of the surface-to-volume ratio is to a tensor quantity that reflects the fact that the nett surface area obstructing molecular motion normal to the orientation of the applied MPG will vary if the medium possesses long-range order in any particular direction. It follows that the coefficients of $\sqrt{\tau}$ calculated from the asparagus data are the EVs of this tensor for that vegetable.

The situation for the long-time limit of the ADT must be similar. That is, rather than using a scalar coefficient depending on the permeability and tortuousity, an extension to a tensor quantity is necessary to describe the results. In this case the physical meaning of the tensor is not immediately clear, but could reflect the fact that the path length between interactions with the obstructing surfaces will on average be longer in certain directions when the tissue is anisotropic at the macroscopic scale. In this case the estimates of the α_{λ_i} from the rat data would correspond to the EVs of that tensor.

Conclusion

OGSE DTI has been applied to in vivo rat brain and clear frequency-dependent alterations to the ADT were observed in all four of the ROIs selected for detailed analysis. The dependence on frequency was approximately linear over the range 33.3–133.3 Hz. All ROIs showed clear increases in MD. While CBWM was the only ROI to show a substantial decrease in FA, the CC and VC had minor increases of the same parameter. All EVs of the ADT tended to increase with MPG frequency in the CBWM, CBGM and VC ROIs, but only the principal EV was found to increase significantly for the CC. Whereas the behaviour of the MD has a simple relationship to the frequency-dependence of the EVs, the relationship between the FA and the EVs with frequency can be most easily understood by redefining the FA to be a function of only two independent variables. It was shown that the FA may either increase or decrease depending on the size of the EVs relative to each other and also on the rates of change of the EVs with frequency. There was no evidence that the orientation of the principal eigenvector of the ADT varied systematically with frequency. Pixelwise linear fits to the MD from individual animals found elevated changes across the cerebellum, suggesting that there may be a contrast in the brains of live animals similar to that discovered in ex vivo brain tissue. It is also worth noting that the ADT was not significantly altered by MPG frequency in a pure water sample, but clear changes were observed due to the presence of microstructure in an asparagus sample. Finally, it is not yet fully understood how the changes to the ADT might be utilised to extract quantitative information about tissue microstructure. A possible interpretation in terms of restricted diffusion and the asymptotic time behaviour of the ADT was discussed, and it was suggested that the asparagus and rat data correspond to the short and long diffusion-time limits, respectively. Histology confirmed that the tissue in each of the ROIs had a different microstructure and therefore the coefficients estimated from the asymptotic diffusion-time behaviour might be used to classify different tissues.

Supplementary data to this article can be found online at http://dx.doi.org/10.1016/j.neuroimage.2012.12.036.

Acknowledgments

The authors would like to thank Sayaka Shibata and Chinami Kajiwara for their assistance with animal care, and Teppei Nakahara and Daisuke Kokuryo for their technical assistance. Thanks are also extended to Professor Kazuhiko Sawada of the Tsukuba International University for helpful discussions. This research was supported by a Grant-in-Aid for Scientific Research (Kakenhi) from the Japan Society for the Promotion of Science (JSPS). It was also partially supported by the JSPS through its "Funding Program for World-Leading Innovative R&D on Science and Technology (FIRST Program)."

References

Aggarwal, M., Jones, M.V., Calabresi, P.A., Mori, S., Zhang, J., 2012. Probing mouse brain microstructure using oscillating gradient diffusion MRI. Magn. Reson. Med. 67, 98–109.

Assaf, Y., Cohen, Y., 1998. Non-mono-exponential attenuation of water and N-acetyl aspartate signals due to diffusion in brain tissue. J. Magn. Reson. 131, 69–85.

Assaf, Y., Freidlin, R.Z., Rohde, G.K., Basser, P.J., 2004. New modeling and experimental framework to characterize hindered and restricted water diffusion in brain white matter. Magn. Reson. Med. 52, 965–978.

Assaf, Y., Blumenfeld-Katzir, T., Yovel, Y., Basser, P.J., 2008. AxCaliber: a method for measuring axon diameter distribution from diffusion MRI. Magn. Reson. Med. 59, 1347–1354.
Basser, P.J., Pierpaoli, C., 1996. Microstructural and physiological features of tissues elucidated by quantitative-diffusion-tensor MRI. J. Magn. Reson. B 111, 209–219.
Basser, P.J., Mattiello, J., Le Bihan, D., 1994. MR diffusion tensor spectroscopy and imaging. Biophys. J. 66, 259–267.
Clark, C.A., Le Bihan, D., 2000. Water diffusion compartmentation and anisotropy at high b values in the human brain. Magn. Reson. Med. 44, 852–859.
Clark, C.A., Hedehus, M., Moseley, M., 2001. Diffusion time dependence of the apparent diffusion tensor in healthy human brain and white matter disease. Magn. Reson. Med. 45, 1126–1129.
Colvin, D.C., Yankeelov, T.E., Does, M.D., Yue, Z., Quarles, C., Gore, J.C., 2008. New insights into tumor microstructure using temporal diffusion spectroscopy. Cancer Res. 68, 5941–5947.
Colvin, D.C., Jourquin, J., Xu, J., Does, M.D., Estrada, L., Gore, J.C., 2011. Effects of intracellular organelles on the apparent diffusion coefficient of water molecules in cultured human embryonic kidney cells. Magn. Reson. Med. 65, 796–801.
de Swiet, T.M., Sen, P.N., 1996. Time-dependent diffusion coefficient in a disordered medium. J. Chem. Phys. 104, 206–209.
Demyanenko, G.P., Schachner, M., Anton, E., Schmid, R., Feng, G., Sanes, J., Maness, P.F., 2004. Close homolog of L1 modulates area-specific neuronal positioning and dendrite orientation in the cerebral cortex. Neuron 44, 423–437.
Does, M.D., Parsons, E.C., Gore, J.C., 2003. Oscillating gradient measurements of water diffusion in normal and globally ischemic rat brain. Magn. Reson. Med. 49, 206–215.
Doran, M., Hajnal, J.V., Van Bruggen, N., King, M.D., Young, I.R., Bydder, G.M., 1990. Normal and abnormal white matter tracts shown by MR imaging using directional diffusion weighted sequences. J. Comput. Assist. Tomogr. 14, 865–873.
Efron, B., Tibshirani, R.J., 1994. An Introduction to the Bootstrap. Chapman & Hall/CRC.
Goodman, J.A., Kroenke, C.D., Bretthorst, G.L., Ackerman, J.J.H., Neil, J.J., 2005. Sodium ion apparent diffusion coefficient in living rat brain. Magn. Reson. Med. 53, 1040–1045.
Grebenkov, D.S., 2007. NMR survey of reflected Brownian motion. Rev. Mod. Phys. 79, 1077–1137.
Gross, B., Kosfeld, R., 1969. Anendung der Spin-Echo-Methode der Messung der Selbstdiffusion. Messtechnik 77, 171–177.
Helmer, K.G., Dardzinski, B.J., Sotak, C.H., 1995. The application of porous-media theory to the investigation of time-dependent diffusion in in vivo systems. NMR Biomed. 8, 297–306.
Horsfield, M.A., Lai, M., Webb, S.L., Baker, G.J., Tofts, P.S., Turner, R., Rudge, P., Miller, D.H., 1996. Apparent diffusion coefficients in benign and secondary progressive multiple sclerosis by nuclear magnetic resonance. Magn. Reson. Med. 36, 393–400.
Kershaw, J., Leuze, C., Autio, J., Shibata, S., Obata, T., Kanno, I., Aoki, I., 2010. Apparent diffusion anisotropy in rat cerebellum is altered at short effective diffusion-times using oscillating-gradient diffusion-tensor MRI. Proceedings of the Joint EUROMAR 2010 and 17th ISMAR Conference, p. 296.
Kershaw, J., Leuze, C., Obata, T., Kanno, I., Aoki, I., 2011. Changes to the fractional anisotropy and mean diffusivity of in vivo rat brain measured at short effective diffusion times. Proceedings of the 19th Annual Meeting of ISMRM, 409.
Latour, L.L., Svoboda, K., Mitra, P.P., Sotak, C.H., 1994. Time-dependent diffusion of water in a biological model system. Proc. Natl. Acad. Sci. U. S. A. 91, 1229–1233.
Latour, L.L., Kleinberg, R.L., Mitra, P.P., Sotak, C.H., 1995. Pore-size distributions and tortuosity in heterogeneous porous media. J. Magn. Reson. 112, 83–91.
Le Bihan, D., Turner, R., Douek, P., 1993. Is water diffusion restricted in human brain white matter? An echo-planar imaging study. Neuroreport 4, 887–890.
Leuze, C.W.U., Anwander, A., Bazin, P.-L., Dhital, B., Stüber, C., Reimann, K., Geyer, S., Turner, R., 2012. Layer-specific intracortical connectivity revealed with diffusion MRI. Cereb. Cortex http://dx.doi.org/10.1093/cercor/bhs311.
Mardia, K.V., Jupp, P.E., 2000. Directional Statistics. Wiley.
Meier, C., Dreher, W., Leibfritz, D., 2003. Diffusion in compartmental systems. II. Diffusion-weighted measurements of rat brain tissue in vivo and postmortem at very large b-values. Magn. Reson. Med. 50, 510–514.
Mitra, P.P., Sen, P.N., Schwartz, L.M., Le Doussal, P., 1992. Diffusion propagator as a probe of the structure of porous media. Phys. Rev. Lett. 24, 3555–3558.
Mitra, P.P., Sen, P.N., Schwartz, L.M., 1993. Short-time behaviour of the diffusion coefficient as geometrical probe of porous media. Phys. Rev. B 47, 8565–8574.
Moonen, C.T.W., Pekar, J., de Vleeschouwer, M.H.M., van Gelderen, P., van Zijl, P.C.M., DesPres, D., 1991. Restricted and anisotropic displacement of water in healthy cat brain and in stroke studied by NMR diffusion imaging. Magn. Reson. Med. 19, 327–332.
Moseley, M., Cohen, Y., Kucharczyk, J., Mintorovitch, J., Asgari, H.S., Wendland, M.F., Tsuruda, J., Norman, D., 1990. Diffusion-weighted MR imaging of anisotropic water diffusion in cat central nervous system. Radiology 176, 439–445.
Niendorf, T., Norris, D.G., Leibfritz, D., 1994. Detection of apparent restricted diffusion in healthy rat brain at short diffusion times. Magn. Reson. Med. 32, 672–677.
Niendorf, T., Dijkhuizen, R.M., Norris, D.G., van Lookeren Campagne, M., Nicolay, K., 1996. Biexponential attenuation in various states of brain tissue: implications for diffusion-weighted imaging. Magn. Reson. Med. 36, 847–857.
Novikov, D.S., Kiselev, V.G., 2011. Surface-to-volume ratio with oscillating gradients. J. Magn. Reson. 210, 141–145.
Parsons, E.C., Does, M.D., Gore, J.C., 2003. Modified oscillating gradient pulses for direct sampling of the diffusion spectrum suitable for imaging sequences. Magn. Reson. Imaging 21, 279–285.
Parsons, E.C., Does, M.D., Gore, J.C., 2006. Temporal diffusion spectroscopy: theory and implementation in restricted systems using oscillating gradients. Magn. Reson. Med. 55, 75–84.
Pfeuffer, J., Provencher, S.W., Gruetter, R., 1999. Water diffusion in rat brain in vivo as detected at very large *b* values is multicompartmental. MAGMA 8, 98–108.
Pilatus, U., Shim, H., Artemov, D., Davis, D., van Zijl, P.C.M., Glickson, J.D., 1997. Intracellular volume and apparent diffusion constants of perfused cancer cell cultures, as measured by NMR. Magn. Reson. Med. 37, 825–832.
Schachter, M., Does, M.D., Anderson, A.W., Gore, J.C., 2000. Measurement of restricted diffusion using an oscillating gradient spin-echo sequence. J. Magn. Reson. 147, 232–237.
Schwartzman, A., Dougherty, R.F., Taylor, J.E., 2005. Cross-subject comparison of principal diffusion direction maps. Magn. Reson. Med. 53, 1423–1431.
Sen, P.N., 2003. Time-dependent diffusion coefficient as a probe of the permeability of the pore wall. J. Chem. Phys. 119, 9871–9876 (erratum 120, 11965–11966).
Sen, P.N., 2004. Time-dependent diffusion coefficient as a probe of geometry. Concepts Magn. Reson. 23A, 1–21.
Sukstanskii, A.L., yablonskiy, D.A., Ackerman, J.J.H., 2004. Effects of permeable boundaries on the diffusion-attenuated MR signal: insights from a one-dimensional model. J. Magn. Reson. 170, 56–66.
Tanner, J.E., 1978. Transient diffusion in a system partitioned by permeable barriers. Application to NMR measurements with a pulsed field gradient. J. Chem. Phys. 69, 1748–1754.
Tuch, D.S., 2004. Q-ball imaging. Magn. Reson. Med. 52, 1358–1372.
Tuch, D.S., Reese, T.G., Wiegell, M.R., Makris, N., Belliveau, J.W., Wedeen, V.J., 2002. High angular resolution diffusion imaging reveals intravoxel white matter fiber heterogeneity. Magn. Reson. Med. 48, 577–582.
van Gelderen, P., de Vleeschouwer, M.H.M., DesPres, D., Pekar, J., van Zijl, P.C.M., Moonen, C.T.W., 1994. Water diffusion and acute stroke. Magn. Reson. Med. 31, 154–163.
Xu, J., Does, M.D., Gore, J.C., 2009. Sensitivity of MR diffusion measurements to variations in intracellular structure: effects of nuclear size. Magn. Reson. Med. 61, 828–833.
Xu, J., Jeong, H.-K., Does, M.D., Anderson, A.W., Chen, L., Gore, J.C., 2010. Dependence of fractional anisotropy on diffusion time: a frequency-domain analysis using temporal diffusion spectroscopy. Proceedings of the 18th Annual Meeting of ISMRM, 4038.
Xu, J., Xie, J., Jourquin, J., Colvin, D.C., Does, M.D., Quaranta, V., Gore, J.C., 2011. Influence of cell cycle phase on apparent diffusion coefficient in synchronized cells detected using temporal diffusion spectroscopy. Magn. Reson. Med. 65, 920–926.
Xu, J., Harkins, K.D., Horch, R.A., Does, M.D., Gore, J.C., 2012. Dependence of temporal diffusion spectroscopy on axon size in white matter tracts of rat spinal cord. Proceedings of the 20th Annual Meeting of ISMRM, 351.

Published OnlineFirst March 26, 2013; DOI: 10.1158/1078-0432.CCR-12-3726

Clinical Cancer Research

Tissue Redox Activity as a Hallmark of Carcinogenesis: From Early to Terminal Stages of Cancer

Rumiana Bakalova, Zhivko Zhelev, Ichio Aoki, et al.

Clin Cancer Res 2013;19:2503-2517. Published OnlineFirst March 26, 2013.

Published OnlineFirst March 26, 2013; DOI: 10.1158/1078-0432.CCR-12-3726

Clinical Cancer Research

Imaging, Diagnosis, Prognosis

Tissue Redox Activity as a Hallmark of Carcinogenesis: From Early to Terminal Stages of Cancer

Rumiana Bakalova[1,2], Zhivko Zhelev[1,3], Ichio Aoki[1], and Tsuneo Saga[1]

Abstract

Purpose: The study aimed to clarify the dynamics of tissue redox activity (TRA) in cancer progression and assess the importance of this parameter for therapeutic strategies.

Experimental Design: The experiments were carried out on brain tissues of neuroblastoma-bearing, glioma-bearing, and healthy mice. TRA was visualized *in vivo* by nitroxide-enhanced MRI on anesthetized animals or *in vitro* by electron paramagnetic resonance spectroscopy on isolated tissue specimens. Two biochemical parameters were analyzed in parallel: tissue total antioxidant capacity (TTAC) and plasma levels of matrix metalloproteinases (MMP).

Results: In the early stage of cancer, the brain tissues were characterized by a shorter-lived MRI signal than that from healthy brains (indicating a higher reducing activity for the nitroxide radical), which was accompanied by an enhancement of TTAC and MMP9 plasma levels. In the terminal stage of cancer, tissues in both hemispheres were characterized by a longer-lived MRI signal than in healthy brains (indicating a high-oxidative activity) that was accompanied by a decrease in TTAC and an increase in the MMP2/MMP9 plasma levels. Cancer progression also affected the redox potential of tissues distant from the primary tumor locus (liver and lung). Their oxidative status increased in both stages of cancer.

Conclusions: The study shows that tissue redox balance is very sensitive to the progression of cancer and can be used as a diagnostic marker of carcinogenesis. The study also suggests that the noncancerous tissues of a cancer-bearing organism are susceptible to oxidative damage and should be considered a therapeutic target. *Clin Cancer Res; 19(9); 2503–17. ©2013 AACR.*

Introduction

Redox signaling plays a crucial role in carcinogenesis (1–4). The increase in cellular oxidants [e.g., reactive oxygen species (ROS) and reactive nitrogen species (RNS)] above a critical level triggers genomic instability and uncontrolled proliferation (1–7), which causes normal cells to become malignant.

Cancer cells are also characterized by an abnormal production of reducing equivalents as a result of accelerated glycolysis (Warburg effect) and the pentose phosphate cycle and by a rapid consumption of these reducers to maintain accelerated anabolism, which is necessary for cell proliferation and immortalization (1, 2, 7, 8). Cancer cells also require high amounts of antioxidants to maintain an ROS/RNS level that is below the threshold for the induction of apoptosis and cell death, but is sufficiently high to ensure genomic instability (1, 7, 9, 10). All of these processes provoke redox imbalance in cancer, which is a hallmark of carcinogenesis. The tissue redox status could be a diagnostic marker, a therapeutic target, and a marker for the evaluation and planning of a therapeutic strategy in real time.

The primary endogenous triggers of redox imbalance in cancer are defective mitochondria and NADPH oxidase complexes. These triggers are involved simultaneously in 2 processes that affect tissue redox status: (i) an excessive generation of ROS (in particular, superoxide and/or hydrogen peroxide) and RNS and (ii) an increased consumption of 3 of the major cellular reducers, as NADH, NADPH, and glutathione (1, 11–18). The high-oxidative activity of cancerous tissue is known despite the hypoxia that occurs in solid tumors. The oxidative capacity of cancer cells is due to abnormal ROS/RNS levels and is not necessarily associated with a high oxygen tension. It is widely accepted that cancer cells are characterized by increased ROS/RNS production compared with that of normal cells that ensure genomic instability (1–15). ROS and RNS are involved in hypoxic signaling pathways and have important implications for the adaptation of cancer to oxidative stress, the induction of uncontrolled proliferation, and immortalization.

Most likely, there is a significant difference between the redox activity of the tumor core and periphery in addition to

Authors' Affiliations: [1]Diagnostic Imaging Program, Molecular Imaging Center, National Institute of Radiological Sciences, Inage-ku, Chiba, Japan, [2]Medical Faculty, Sofia University "St. Kliment Ohridski", Sofia; and [3]Medical Faculty, Trakia University, Stara Zagora, Bulgaria

Corresponding Author: Rumiana Bakalova, National Institute of Radiological Sciences, 4-9-1 Anagawa, Inage, Chiba 263-8555, Japan. Phone: 81-43-206-4067; Fax: 81-43-206-4067; E-mail: bakalova@nirs.go.jp

doi: 10.1158/1078-0432.CCR-12-3726

Published OnlineFirst March 26, 2013; DOI: 10.1158/1078-0432.CCR-12-3726

Translational Relevance

This study directly relates to cancer diagnosis, the assessment of cancer progression (from early to terminal stage), and planning a therapeutic strategy. This study shows that tissue redox balance is very sensitive to cancer development and can be used as a diagnostic marker of carcinogenesis. The method is simple and applicable on isolated tissue and blood specimens. The method shows the potential for promising application in molecular imaging diagnostic *in vivo* on humans following the development of cell-penetrating nitroxide probes with high contrast, low toxicity, and minimal side effects.

The most important observations are that the oxidative status of noncancerous tissues (even those distant from the primary tumor locus) increases with cancer progression and that these tissues become susceptible to oxidative stress and damage.

tumors in different stages (i.e., early, intermediate, and terminal) of development. However, there are methodologic restrictions that hamper the visualization and evaluation of such a difference *in vivo*. There is no suitable sensor platform for real-time imaging of tissue redox activity (TRA) that is characterized by high sensitivity and resolution.

Recently, we reported a noninvasive methodology for the estimation of TRA on intact mammals, allowing a differentiation of cancer development from normal (healthy) conditions (19–21). The method is based on the redox cycle of cell-penetrating nitroxide derivatives and their MRI and electron paramagnetic resonance (EPR) contrast properties, which make them useful molecular sensors for TRA (Fig. 1).

In vitro studies indicate that the contrast-enhancing nitroxide radical could be converted rapidly to the noncontrast-enhancing hydroxylamine and/or oxoammonium by different cellular compounds (e.g., free ions of transition metals, hydroxyl and hydroperoxyl radicals, ubiquinols, NAD(P)H, and ascorbate/dehydroascorbate; Fig. 1; refs. 22–28). In turn, hydroxylamine and oxoammonium are "superoxide dismutase mimetics" and could restore the nitroxide radical (22, 26, 29). The logarithmic acid dissociation constant value of 4.8 is reported for the equilibrium between superoxide anion and its protonated form, that is, the hydroperoxyl radical. The interaction of oxoammonium with superoxide occurs at pH < 4.5, whereas under physiologic conditions (pH ~ 7.4) the oxoammonium is reduced to hydroxylamine by NAD(P)H (26). The interaction of hydroxylamine with superoxide occurs at approximately pH 7.4 with the release of hydrogen peroxide and restoration of the radical form of the nitroxide (26). Ui and colleagues have reported that the exposure to hydrogen peroxide inhibits the reduction of the nitroxide radical *in vivo*, and hydrogen peroxide reoxidizes hydroxylamine to the original radical form (22, 30). It seems that *in vivo*, nitroxide exists primarily in 2 forms: as a radical and as hydroxylamine. Various reducers and oxidizers are involved (directly or indirectly) in the formation of hydroxylamine, but only the interaction of hydroxylamine with superoxide and/or hydrogen peroxide seems to dominate *in vivo* as the process that restores the nitroxide radical and its MRI/EPR contrast.

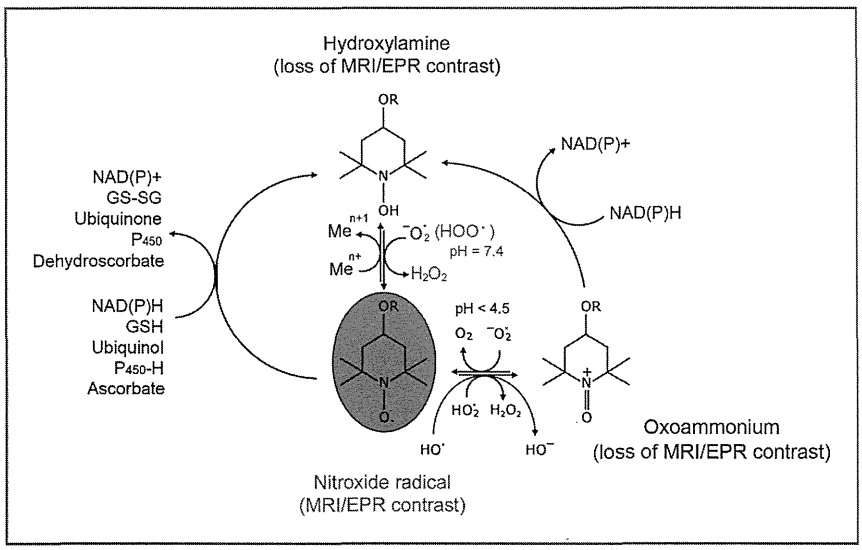

Figure 1. Nitroxide redox cycle as a sensing platform for the imaging of TRA: principle of the method. *In vitro* studies show that the nitroxide radical, which is characterized by MRI/EPR contrast enhancement, can be converted to the noncontrast hydroxylamine and/or oxoammonium by different compounds in cells and body fluids (e.g., free ions of transition metals, hydroxyl and hydroperoxyl radicals, ubiquinols, NAD(P)H, ascorbate, glutathione, etc.). The contrast-enhancing radical form can be recovered by interaction of hydroxylamine with the superoxide radical at physiologic, pH (7.4), or interaction of oxoammonium with the superoxide radical at pH < 4.5. Thus, the nitroxide-enhanced MRI/EPR signal follows the reduction/oxidation of the nitroxide derivative and indicates the redox status of tissues and body fluids.

Published OnlineFirst March 26, 2013; DOI: 10.1158/1078-0432.CCR-12-3726

Briefly, the nitroxide radical participates in electron transfer reactions with oxidizers and reducers with the formation of contrast-enhancing or noncontrast intermediate products (31–33). The rate constants of these reactions determine the intensity of the nitroxide-enhanced MRI/EPR signal in living cells and tissues. In healthy mammals, the intensity, duration, and/or half-life of the nitroxide-enhanced MRI/EPR signal ($\tau_{1/2}$) in the selected region of interest (ROI; e.g., cells, tissues, bloodstream) can be considered a reference value for the redox activity of the respective specimen in normal conditions (healthy organism; ref. 19). Any significant deviation from this reference value indicates a redox imbalance, such as the high-oxidative or reducing activity of cells, tissues, or physiologic fluids. In previous studies, we established that in cancer-bearing mammalian tissues, the intensity, duration, and $\tau_{1/2}$ values were completely different from the respective reference values and that this parameter is a valuable diagnostic marker for carcinogenesis (19–21).

The EPR contrast of the nitroxide radical allows the determination of the exact concentration and redox status of the nitroxide derivative in the respective tissue and/or cells using EPR spectroscopy or imaging (EPRI; refs. 31–35). The comparative analysis of the results, obtained using both imaging techniques, gives accurate information about the TRA *in vivo*.

The reduction/oxidation of nitroxide is spatially separated and occurs in (i) the bloodstream, (ii) the extracellular–extravascular space (EES) of the tissue, and (iii) the cells of the tissue. The MRI/EPR signal dynamics is a result of various factors and processes that occur simultaneously in the following 4 areas: (i) the lifetime of the nitroxide in the circulation, depending on its water solubility (35, 36), (ii) the reduction/oxidation of the nitroxide in the bloodstream, which is expected to be low in the plasma but sufficiently high in blood cells (if it penetrates cell membranes; refs. 35, 36), (iii) the penetration and accumulation of the nitroxide in the EES and its reduction/oxidation, which is expected to be negligible, and (iv) the penetration and accumulation of the nitroxide in the cells of the tissue and its intracellular reduction/oxidation, which is expected to be substantial in comparison with the bloodstream and EES (20, 37). TRA is a combination of the redox capacity of the extracellular (EES) and intracellular space of the tissue. The metabolism and/or clearance of nitroxide from the organism is not related to the redox activity of the tissues and physiologic fluids and should be negligible during short-term scanning.

The hydrophilic nitroxides are characterized by a long lifetime in the circulation and a very slow penetration or no penetration into the cells. In contrast, the hydrophobic (and amphiphilic) nitroxides are characterized by a short lifetime in the circulation and an easy penetration into the EES and cells. Therefore, only the hydrophobic cell-penetrating nitroxides are appropriate molecular sensors for MRI/EPRI of TRA, especially *in vivo*.

This study aims to clarify the difference between TRAs in different stages of cancer development *in vivo*. For this purpose, we used 2 cancer models (neuroblastoma- and glioma-bearing mice), blood–brain barrier (BBB)-penetrating and cell-penetrating nitroxide derivatives, and nitroxide-enhanced MRI and EPR spectroscopy.

Materials and Methods

Chemicals

2,2,6,6-tetramethylpiperidine-1-oxyl–labeled nitrosourea (SLENU) was synthesized according to the procedure described by Gadjeva (38). SLENU is a spin-labeled analog of the conventional anticancer drug 1-(2-chloroethyl)-3-cyclohexyl-1-nitrosourea (Lomustine). 4-hydroxy-2,2,6,6-tetramethylpiperidine 1-oxyl (TEMPOL) was purchased from Sigma-Aldrich (cat. No. 176141).

Cancer models and experimental design

All experiments were carried out in accordance with the guidelines of the Physiological Society of Japan and were approved by the Animal Care and Use Committee of the National Institute of Radiological Sciences (NIRS; Chiba, Japan).

The mice (nude *Balb/c*; male) were separated into the following groups: healthy mice (controls) and cancer-bearing mice with brain neuroblastoma or glioma. In all groups, the mice were of identical age, nearly identical weight (23 ± 3 g), and maintained under identical conditions.

Two cancer models were developed using *Neuro2a* (neuroblastoma) or *U87* (glioma) cells. Cancer cells (0.5×10^5 cells in 10 μL) were grafted in one hemisphere of the brain. Anatomically visualized brain neuroblastoma or glioma developed within approximately 9 or 20 days after inoculation, respectively.

The mice were subjected to MRI measurements on the third and ninth day after the inoculation of *Neuro2a* cells or on the seventh and 20th day after inoculation of *U87* cells, when the cancer was in the early and intermediate/terminal stage of its development, respectively.

In preliminary experiments, we investigated the effect of "sham tumor inoculation" (using 10 μL of PBS) on the dynamics of the nitroxide-enhanced MRI signal. Because there was no difference between inoculated and noninoculated hemispheres, or between untreated healthy mice and mice with "sham tumor inoculation," we used untreated healthy mice as controls in this study.

In vivo MRI measurements

MRI measurements were conducted on a 7.0 Tesla horizontal magnet (Kobelco and Jastec) interfaced to a Bruker Avance console (Bruker BioSpin) and controlled with the ParaVision 4.0.1 program (Bruker BioSpin).

The mice were anesthetized by isoflurane (1.2%) and placed in a head or body holder (RAPID Biomedical). A respiration sensor (SA Instruments Inc.) was placed on the back of the mice. A temperature probe (FOT-M and FTI-10, FISO Technologies Inc.) was used to monitor the rectal temperature. The tail vein was cannulated using a polyethylene tube (PE-10, Becton-Dickinson) for the drug injection. The mouse was placed in the ^{1}H-volume

Published OnlineFirst March 26, 2013; DOI: 10.1158/1078-0432.CCR-12-3726

radio-frequency resonator (Bruker BioSpin) with surface radio-frequency receiver (RAPID Biomedical), which was prewarmed using a body temperature controller (RAPID Biomedical). The resonator units, including the mouse, were placed in the magnet bore. The body temperature was maintained at 37 ± 1°C during the MRI measurements.

Five control images of the mouse brain or body were taken before injection with the following parameters: T_1-weighted incoherent gradient-echo sequence (fast low-angle shot), repetition time = 75 ms; echo time = 3.5 ms; flip angle = 45°; field of view = 3.2 × 3.2 cm; number of averages = 4; scan time = 19.6 seconds; matrix = 64 × 64; slice thickness = 1.0 mm; and number of slices = 4. A solution of nitroxide derivative [SLENU, dissolved in dimethyl sulfoxide (DMSO), or TEMPOL, dissolved in 10 mmol/L PBS, pH 7.4, and reduced by ascorbate, 1:1, mol:mol; 100 mmol/L stock solutions] was injected via the tail vein (100 μL/25 g mouse; 0.4 μmol/g body weight) 1 minute and 40 seconds after beginning the scan. T_1-weighted images were acquired continuously within approximately 14 minutes, using the parameters described above. Mice injected with DMSO served as negative controls. DMSO did not act as a radical scavenger under the experimental conditions described above. TEMPOL, dissolved in DMSO, produced an identical nitroxide-enhanced MRI signal (as intensity and profile) in anesthetized mice as TEMPOL dissolved in PBS. The final dose of each nitroxide was lower than the LD_{50} value calculated for intravenous administration in wild-type mice (38).

The MRI data were analyzed using ImageJ software (NIH, Bethesda, MD). The averaged value of the first 5 control sequences (recorded before injection) was calculated, and each sequence of the kinetic measurement was normalized to this averaged value by division using an identical algorithm to that presented by Zhelev and colleagues (39).

In vitro EPR measurements

The mice were euthanized, and the brain, lung, and liver were isolated. The tissues were homogenized in a 4-fold volume of PBS. Protein concentration was measured using the Bradford method, and each homogenate was diluted to 10 mg protein/mL. Noncontrast-enhancing reduced TEMPOL (dissolved in 10 mmol/L PBS, pH 7.4, and reduced by ascorbate; 1:1, mol:mol) was added to the tissue homogenate (final concentration of TEMPOL: 10 mmol/L). The sample (100 μL) was placed into a glass capillary, and X-band EPR spectra were recorded on an X-band EPR instrument (Bruker) with a transverse electric–mode cavity. The measurements were conducted under the following conditions: microwave frequency = 9.4 GHz; magnetic field strength = 336 mT; microwave power = 2.0 mW; field modulation frequency = 100 kHz; field modulation amplitude = 0.063 mT; time constant = 0.01 seconds; sweep width = 10 mT; and scan time (sweep time) = 1 minute (39). The EPR spectra were recorded before and after the addition of reduced TEMPOL. The data were normalized to 1 mg protein/mL.

In vitro total antioxidant capacity assay

The total antioxidant capacity (TAC) in isolated tissue homogenates was analyzed using the OxiSelect Total Antioxidant Capacity Assay Kit (Cell Biolabs Inc.), according to the manufacturer's instructions. The samples were analyzed photometrically at 490 nm using the microplate reader "Tecan Infinite F200 PRO" (Tecan Austria GmbH).

Analysis of plasma MMP2 and MMP9 levels

The plasma samples were obtained from healthy and neuroblastoma-bearing mice. ELISA was used to determine plasma total matrix metalloproteinases (MMP)2 and total MMP9 levels, according to the manufacturer's instructions. The MMP2 ELISA Kit [Human/Mouse/Rat MMP2 (total), Quantikine; R&D Systems Inc.] detects pro-, active, and tissue inhibitor of metalloproteinase (TIMP)-complexed MMP2. The MMP9 ELISA Kit [Mouse MMP9 (total), Quantikine; R&D Systems Inc.] detects pro-, active, and TIMP-complexed MMP9.

Statistical analysis

The data were statistically analyzed by ANOVA using Student *t* test.

Results

Early stage of brain neuroblastoma

Figure 2 shows typical images of the extracted nitroxide-enhanced MRI signal (normalized to the baseline) in healthy (Fig. 2A) and neuroblastoma-bearing mice in the early stage of cancer (3 days after inoculation of cancer cells into the brain; Fig. 2B). In this stage, the tumor cannot be detected anatomically even with high- resolution MRI (spin-echo sequence). The images from both experimental groups were similar. The averaged kinetic curves, however, showed that there was a significant difference in the duration and half-life ($\tau_{1/2}$) of the nitroxide-enhanced MRI signal between control and neuroblastoma-bearing mice (Fig. 2C and D).

Two ROIs were selected: (i) the brain area (ROI1) and (ii) the surrounding (nonbrain) area (ROI2; Fig. 2A, a). In both ROIs, the signal increased after the injection of nitroxide followed by a rapid or slower decrease to the baseline. The enhancement of the MRI signal in the beginning is due to the presence of nitroxide in the blood and its penetration and accumulation in the subsequent tissue, whereas the decrease is due to its reduction to noncontrast hydroxylamine, which occurs predominantly in cells.

In the brain area (ROI1) of healthy mice, the half-life of the nitroxide-enhanced MRI signal ($\tau_{1/2}$) was approximately 80 seconds and the duration of the signal was approximately 5 minutes and 40 seconds, and these values can be considered a reference for the TRA of the normal brain (Fig. 2C, gray curve). The profile of the histograms indicates a high reducing activity of normal brain tissue for the nitroxide radical. In ROI1 of neuroblastoma-bearing mice, $\tau_{1/2}$ was approximately 56 seconds and the duration of the signal was approximately 3 minutes, which is significantly

Published OnlineFirst March 26, 2013; DOI: 10.1158/1078-0432.CCR-12-3726

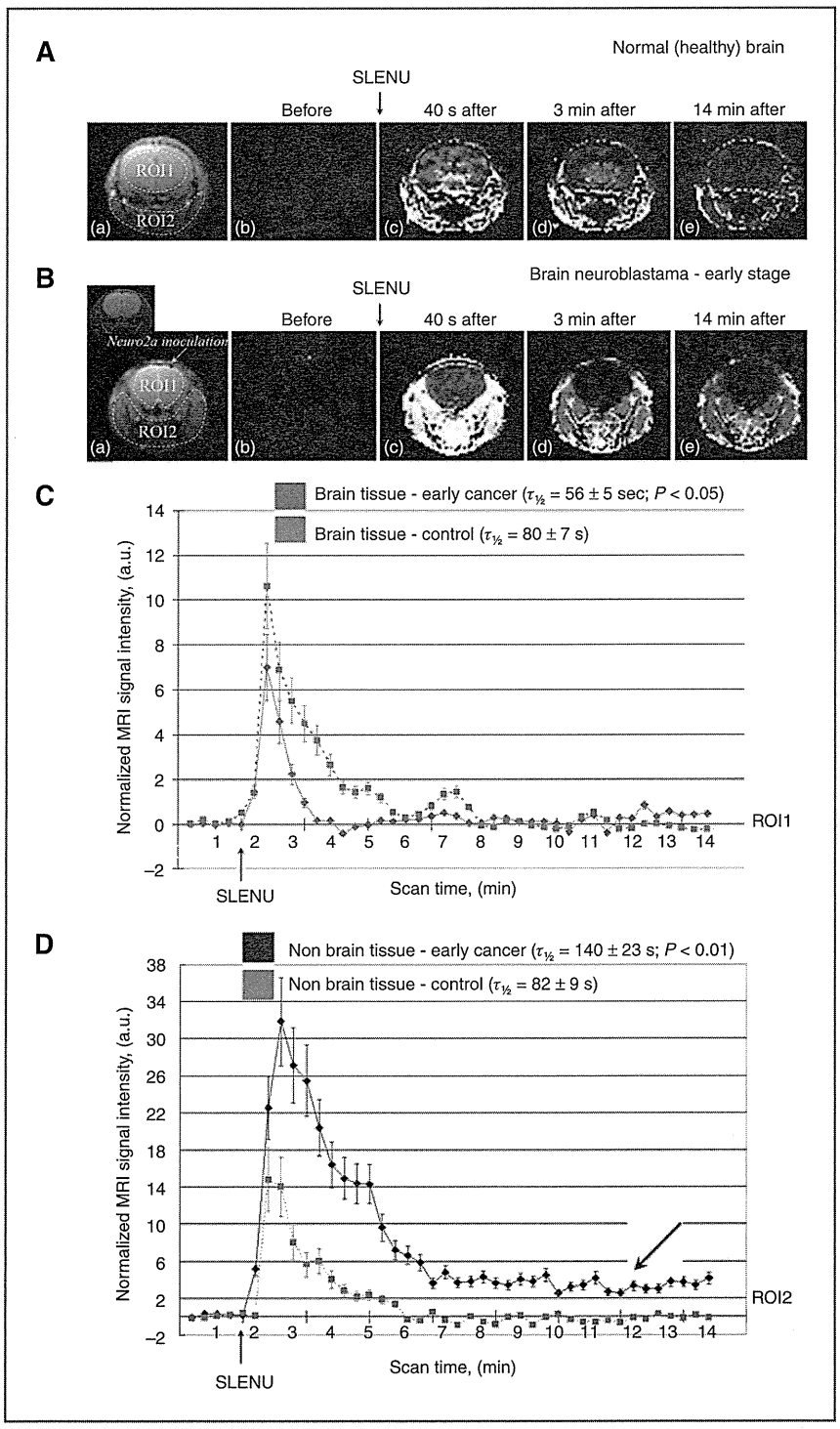

Figure 2. Healthy and neuroblastoma-bearing mice (early stage of cancer development). A and B, typical MR images of healthy brain (A) and neuroblastoma-bearing brain in the early stage of cancer (B): a, MR image of mouse brain; b, extracted nitroxide-enhanced MRI signal obtained before (baseline; b); and after injection of nitroxide (SLENU; c, d, e). C and D, kinetics of the nitroxide-enhanced MRI signal in the brain (ROI1; C) and surrounding (nonbrain) tissues (ROI2; D) obtained before and after injection of SLENU. Control kinetics (gray dotted lines) obtained in healthy mice are given for comparison. The data are the mean ± SD from 10 animals for the control group and 7 animals for the neuroblastoma-bearing group. ROIs are indicated by dotted lines on MR images. SLENU was in the oxidized (radical) form.

Published OnlineFirst March 26, 2013; DOI: 10.1158/1078-0432.CCR-12-3726

shorter than that of control mice ($P < 0.05$; Fig. 2C, red curve). This result indicates that the reducing capacity of the brain tissue in the early stage of brain neuroblastoma was higher than that of the control brain.

In the surrounding (nonbrain) tissues (ROI2), the opposite tendency was observed (Fig. 2D). In healthy mice, the half-life of the MRI signal was significantly shorter than that in the neuroblastoma-bearing mice; approximately 82 seconds versus approximately 140 seconds, respectively ($P < 0.01$). The duration of the signal in neuroblastoma-bearing mice was more than 14 minutes versus 5 minutes and 40 seconds in healthy mice. This result indicates that the reducing activity of nonbrain tissues in the early stage of neuroblastoma is lower than that in the control group. In neuroblastoma-bearing mice, the MRI signal did not reach the baseline within 14 minutes of continuous scanning (Fig. 2D, blue curve), which indicates that the oxidation of nitroxide dominates over reduction.

Terminal stage of brain neuroblastoma

In the terminal stage of brain neuroblastoma (9 days after inoculation), the kinetics of the nitroxide-enhanced MRI signal in the brain and nonbrain tissues were completely different from the reference profiles, recorded for the control group, and from the profiles of the early neuroblastoma group (Fig. 3B and C). Three ROIs were selected: (i) the cancerous hemisphere (ROI1), (ii) the noncancerous hemisphere (ROI2), and (iii) the surrounding (nonbrain) area (ROI3; Fig. 3A, a). The cancer was visualized anatomically by MRI.

In ROI1 and ROI2, the signal increased after injection and reached a plateau without a decrease within 14 minutes ($\tau_{1/2} > 14$ minutes; $P < 0.001$ vs. control). In ROI3, the signal increased after injection then decreased slowly without reaching the baseline within 14 minutes ($\tau_{1/2} \sim 14$ minutes; $P < 0.001$ vs. control). The histograms indicate a high-oxidative activity of the cancerous and noncancerous tissues of neuroblastoma-bearing mice for the nitroxide. In all ROIs of neuroblastoma-bearing mice, the duration of the signal was more than 14 minutes versus 5 minutes and 40 seconds in controls.

The kinetics of the MRI signal showed identical profiles in both hemispheres of the neuroblastoma-bearing brain (Fig. 3B); however, the signal intensity was significantly higher in the cancerous area than in the noncancerous hemisphere (Figs. 2B and 3A).

Early stage of brain glioma

Figure 4A shows a typical image of brain glioma in the early stage of development (9 days after the inoculation of cancer cells into the brain). The tumor is very small but can be visualized anatomically using high-resolution MRI (spin-echo sequence). Two ROIs were selected: (i) the brain area (ROI1) and (ii) the surrounding (nonbrain) area (ROI2; Fig. 4A).

In ROI1 of glioma-bearing mice, the half-life of the MRI signal decay was significantly shorter than that in control mice ($\sim$63 seconds vs. 80 seconds, respectively; $P < 0.05$); the duration of the signal was approximately 3 minutes versus approximately 5 minutes and 30 seconds in controls (Fig. 4B, red curve). This result indicates that the reducing activity of the brain tissue in the early stage of brain glioma is higher than that of the control brain.

In the surrounding tissues (ROI2), an opposite tendency was observed (Fig. 4C). In healthy mice, the half-life of the MRI signal was significantly shorter than that in the glioma-bearing mice; approximately 82 seconds versus approximately 180 seconds, respectively ($P < 0.01$). The duration of the signal in glioma-bearing mice was more than 14 minutes versus approximately 5 minutes and 40 seconds in control mice. This result indicates that the reducing activity of nonbrain tissues in the early stage of brain glioma is lower than that in the control group. In glioma-bearing mice, the MRI signal did not reach the baseline within 14 minutes of continuous scanning (Fig. 4C, blue curve), which indicates that the oxidation of nitroxide dominates over reduction.

Terminal stage of brain glioma

In the terminal stage of brain glioma (20 days after inoculation), the kinetics of the nitroxide-enhanced MRI signal in the brain and nonbrain tissues were completely different from the reference profiles that were recorded for the control group (Fig. 5B and C). Three ROIs were selected: (i) the cancerous hemisphere (ROI1), (ii) the noncancerous hemisphere (ROI2), and (iii) the surrounding (nonbrain) area (ROI3; Fig. 5A, a). The cancer was visualized anatomically by MRI.

In ROI2, the signal increased after injection and reached a plateau without a decrease within 14 minutes ($\tau_{1/2} > 14$ minutes; $P < 0.001$ vs. control). In ROI1 and ROI3, the signal increased after injection then decreased slowly without reaching the baseline within 14 minutes (in ROI3: $\tau_{1/2} \sim 440$ seconds; $P < 0.001$ vs. control; in ROI2: $\tau_{1/2} \sim 330$ seconds; $P < 0.001$ vs. control). The histograms indicate a high-oxidative activity of the cancerous and noncancerous tissues of glioma-bearing mice for the nitroxide.

The kinetics of the MRI signal showed identical profiles in both hemispheres of the glioma-bearing brain. However, the signal intensity was significantly higher in the cancerous area than in the noncancerous hemisphere (Fig. 5A, b).

Tissue-oxidizing capacity *in vivo* and *in vitro*

To verify the data from the nitroxide-enhanced MRI *in vivo*, we used a second experimental strategy. Nitroxide (TEMPOL) was reduced until there was a complete loss of the MRI and EPR contrast. The reduced noncontrast-enhancing form was injected in anesthetized mice (healthy and cancer bearing), and the dynamics of the nitroxide-enhanced MRI signal were detected under identical conditions, as in Figs. 2 and 3.

The data in Fig. 6A indicate that the nitroxide-enhanced MRI signal appeared and increased within 14 minutes of continuous scanning only in the brain of neuroblastoma-bearing mice in the terminal stage of cancer (red and yellow curves). The signal intensity was higher in the cancerous hemisphere than in the noncancerous hemisphere. In the

Published OnlineFirst March 26, 2013; DOI: 10.1158/1078-0432.CCR-12-3726

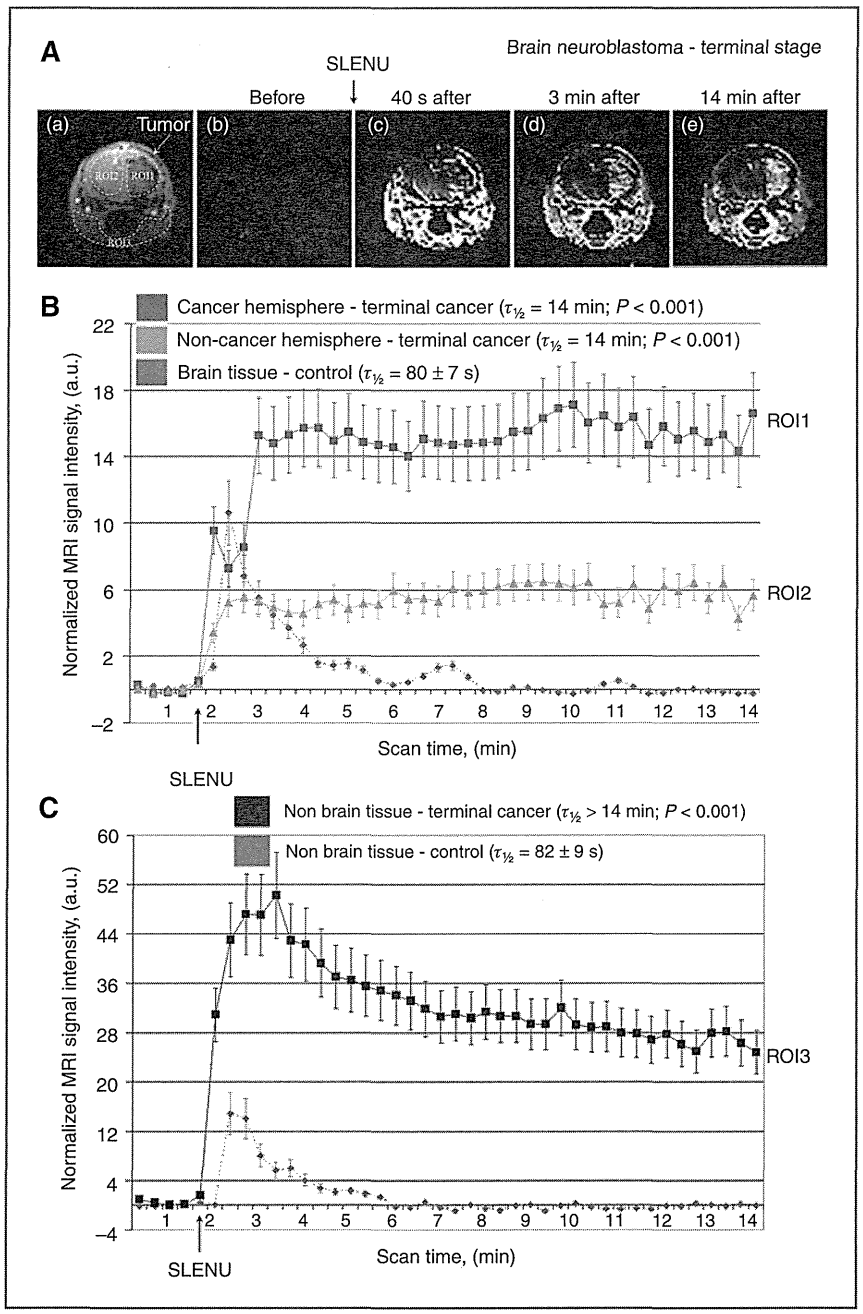

Figure 3. Healthy and neuroblastoma-bearing mice (terminal stage of cancer development). A, typical MR images of neuroblastoma-bearing brain in the terminal stage of cancer: a, MR image of mouse brain; b, extracted nitroxide-enhanced MRI signal obtained before (baseline; b) and after injection of nitroxide (SLENU; c, d, e). B and C, kinetics of the nitroxide-enhanced MRI signal in the brain, cancerous hemisphere (ROI1), and noncancerous hemisphere (ROI2; B), and surrounding (nonbrain) tissues (ROI3; C) obtained before and after injection of SLENU. Control kinetics (gray dotted lines) obtained in healthy mice are given for comparison. The data are the mean ± SD from 10 animals for each group. ROI are indicated by dotted lines on MR images. SLENU was in the oxidized (radical) form.

controls and early-stage neuroblastoma, the nitroxide-enhanced MRI signal was not detected (violet and gray curves). The kinetic measurements obtained with injection of oxidized TEMPOL are shown for comparison in Fig. 6B. The dynamics were characterized by an initial peak as a result of the accumulation of nitroxide in the brain. For healthy mice or mice with early neuroblastoma, the signal decreased rapidly to the baseline. For mice with terminal neuroblastoma, the signal remained high in both hemispheres.

The results suggest that the noncontrast reduced nitroxide was converted to its contrast-enhancing oxidized form only by the tissues of the neuroblastoma-bearing mice in the terminal stage of cancer. This experimental design proves

Published OnlineFirst March 26, 2013; DOI: 10.1158/1078-0432.CCR-12-3726

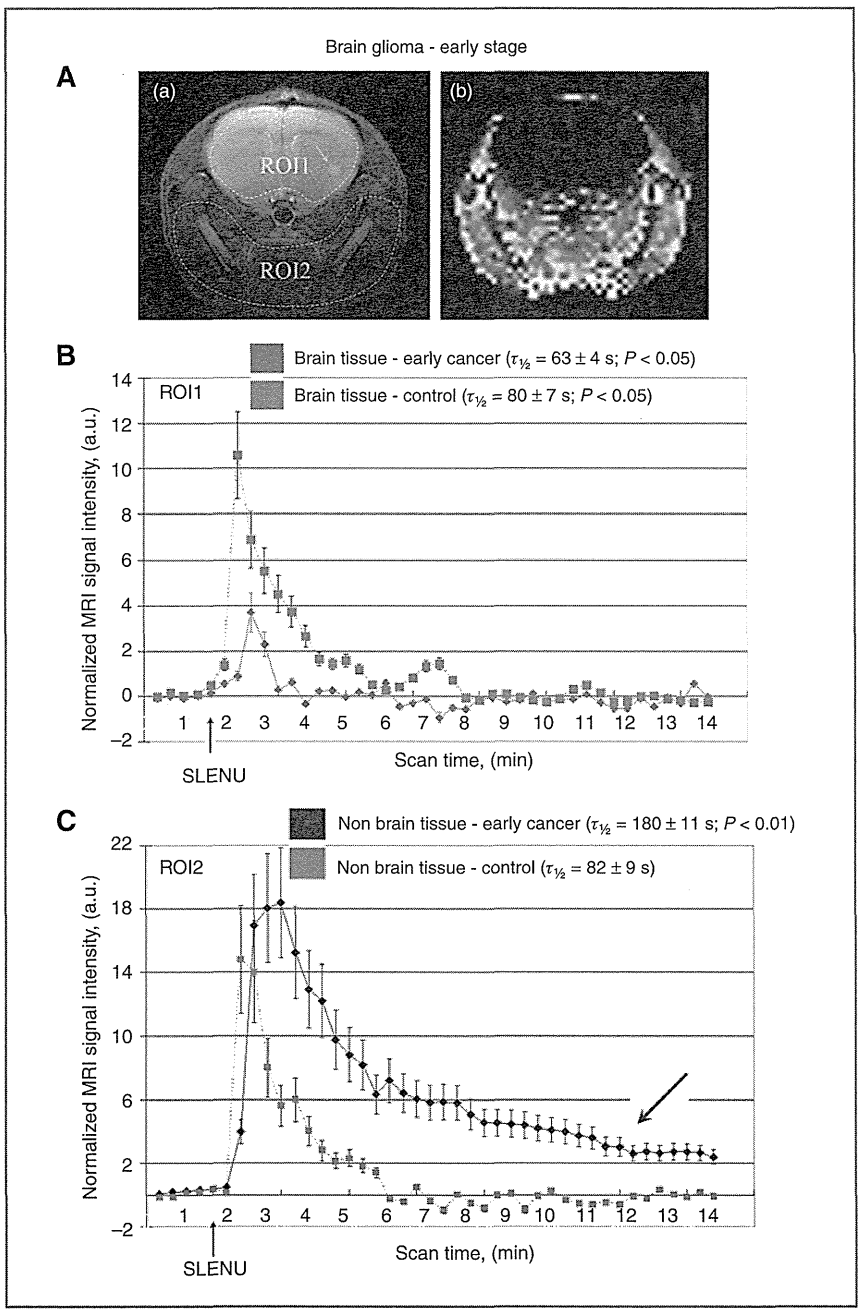

Figure 4. Healthy and glioma-bearing mice (early stage of cancer development). A, typical MR image of glioma-bearing mouse brain in the early stage of cancer: a, MR image of mouse brain; b, extracted nitroxide-enhanced MRI signal obtained 3 minutes after injection of nitroxide (SLENU). B and C, kinetics of the nitroxide-enhanced MRI signal in the brain (ROI1; B) and surrounding (nonbrain) tissues (ROI2; C) obtained before and after injection of SLENU. Control kinetics (gray dotted lines) obtained in healthy mice are given for comparison. The data are the mean ± SD from 10 animals for the control group and 5 animals for the glioma-bearing group. ROIs are indicated by dotted lines on the MR image. SLENU was in the oxidized (radical) form.

that these tissues are characterized by high-oxidative activity, which is not typical for tissues of healthy mice or neuroblastoma-bearing mice in the early stage of cancer.

Similar data were obtained *in vitro* using tissue specimens (brain, liver, and lung) and EPR spectroscopy (Fig. 6C). The tissues were isolated from healthy or neuroblastoma-bearing mice in the early or terminal stage of cancer. A reduced noncontrast nitroxide was added to each sample, and the appearance of the EPR spectra was detected after 10 minutes of incubation at room temperature. The appearance of EPR spectra is a result of the conversion of nitroxide probe from the reduced to oxidized (radical) form and is indicative of high-oxidative activity of the respective tissue. The EPR triplet appeared in all tissues of neuroblastoma-bearing

Published OnlineFirst March 26, 2013; DOI: 10.1158/1078-0432.CCR-12-3726

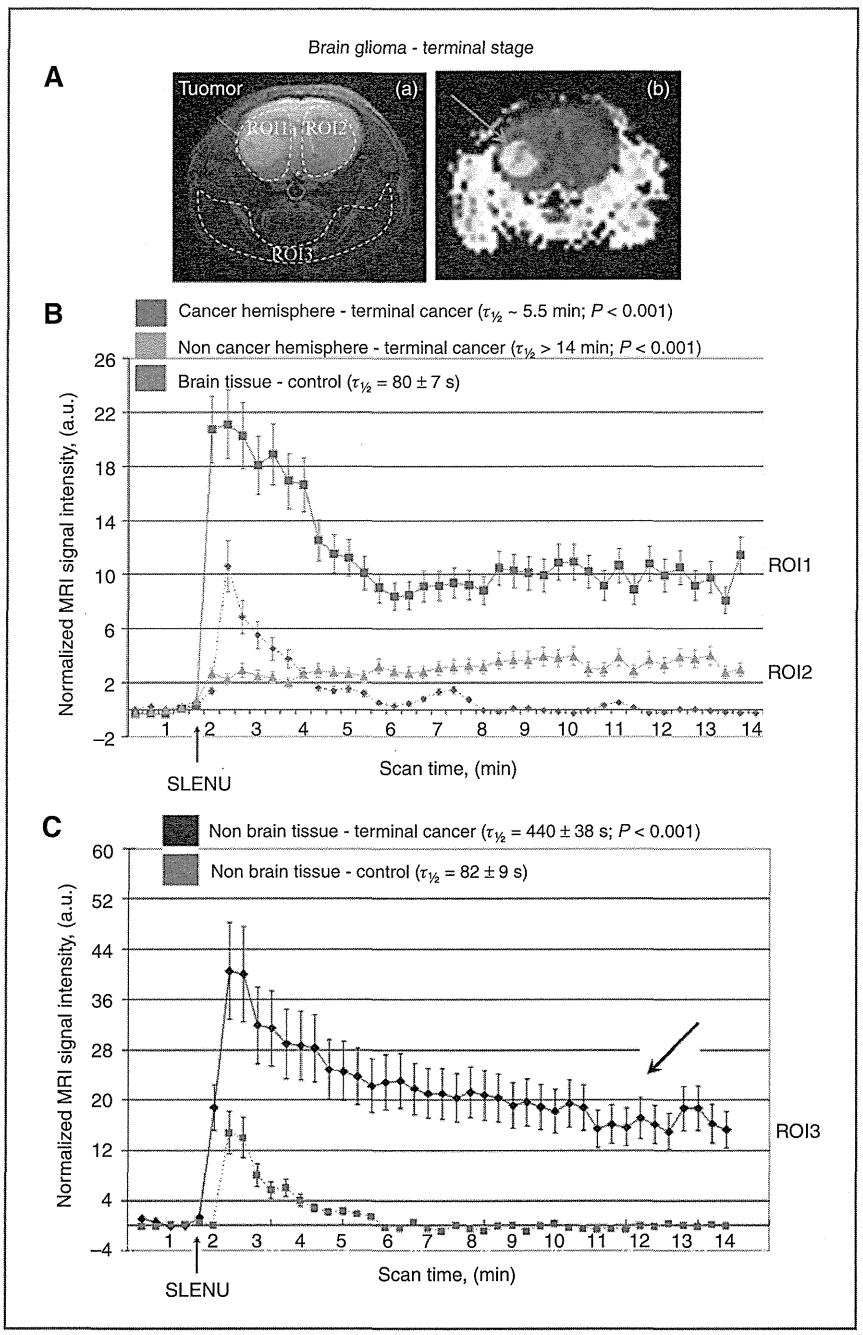

Figure 5. Healthy and glioma-bearing mice (terminal stage of cancer development). A, typical MR image of glioma-bearing mouse brain in the terminal stage of cancer: a, MR image of mouse brain; b, extracted nitroxide-enhanced MRI signal obtained 3 minutes after injection of nitroxide (SLENU). B and C, kinetics of the nitroxide-enhanced MRI signal in the brain, cancerous hemisphere (ROI1), and noncancerous hemisphere (ROI2; B), and surrounding (nonbrain) tissues (ROI3; C) obtained before and after injection of SLENU. Control kinetics (gray dotted lines) obtained in healthy mice are given for comparison. The data are the mean ± SD from 10 animals for the control group and 7 animals for the glioma-bearing group. ROIs are indicated by dotted lines on the MR image. SLENU was in the oxidized (radical) form.

mice in the terminal stage of cancer and in the liver of neuroblastoma-bearing mice in the early stage of cancer. This result indicates that all of these tissues are characterized by high-oxidative activity for the nitroxide probe. The cancerous hemisphere was characterized by the highest tissue-oxidative capacity.

Total antioxidant capacity of brain tissue and plasma levels of matrix metalloproteinases

To investigate the potential molecular mechanism(s) of redox imbalance in cancer-bearing mice, we analyzed 2 biochemical parameters: (i) the TAC of brain tissue and (ii) the plasma levels of the MMPs, MMP2 and MMP9.

Published OnlineFirst March 26, 2013; DOI: 10.1158/1078-0432.CCR-12-3726

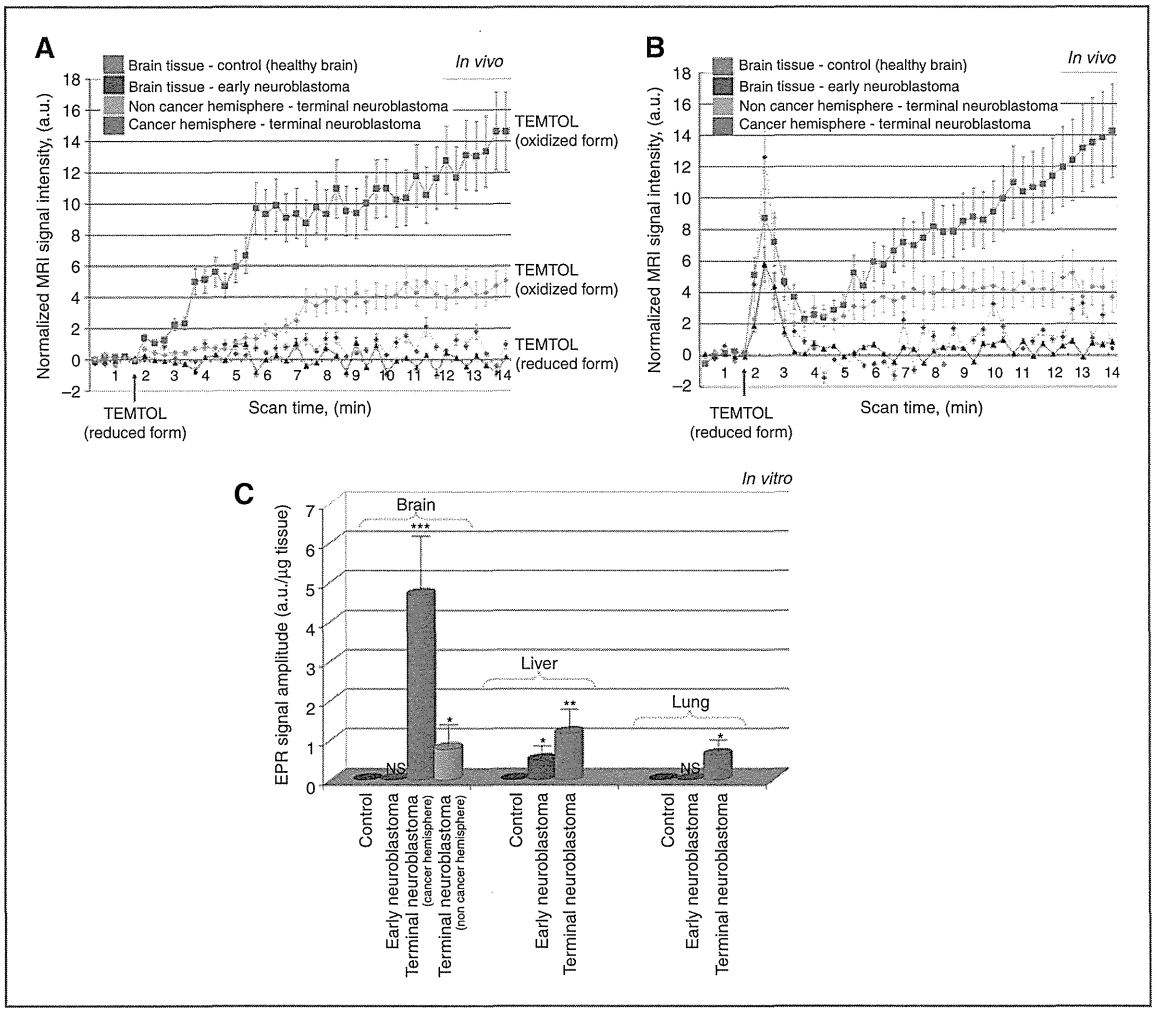

Figure 6. Analysis of the tissue oxidizing capacity *in vivo* and *in vitro* in healthy and neuroblastoma-bearing mice in the early and terminal stage of cancer. A, kinetics of the nitroxide-enhanced MRI signal in the brain before and after injection of reduced nitroxide (TEMPOL). The data are the mean ± SD from 4 animals for each group. B, kinetics of the nitroxide-enhanced MRI signal in the brain before and after injection of oxidized nitroxide (TEMPOL). The data are the mean ± SD from 6 animals for the control group and 4 animals for all other groups. C, amplitude of the EPR signal in isolated tissue specimens after addition of reduced TEMPOL. The data are the mean ± SD from 4 animals for each group. *, $P < 0.05$; **, $P < 0.01$; ***, $P < 0.001$.

It was established that the TAC of brain tissue slightly increased (~20%) in the early stage of cancer, whereas in the terminal stage, it markedly decreased (~40%) in comparison with the control (Fig. 7A). The plasma total MMP2 and MMP9 levels were significantly higher in neuroblastoma-bearing mice in the terminal stage of cancer than those in healthy mice (Fig. 7B). The plasma MMP9, but not MMP2, level also increased in neuroblastoma-bearing mice in the early stage of cancer.

Discussion

The data show 2 important trends in carcinogenesis: (i) the tissues of cancer-bearing mammals (cancerous and noncancerous, including areas distant from the primary tumor locus) are characterized by high-oxidative activity, whereas the tissues of a healthy organism are characterized by high-reducing activity for the nitroxide and (ii) the tissue redox balance is very sensitive to the progression of cancer: in the early stage, reduction dominates over oxidation, whereas in the terminal stage, oxidation dominates over reduction. Our additional experiments on colon cancer-grafted mice treated with camptothecin within 3 weeks showed a suppression of tumor growth and significant normalization of tissue reducing potential compared with the placebo group (data to be published elsewhere).

Similar results have been reported by Matsumoto and colleagues and Hyodo and colleagues (22, 23). The authors have investigated the dynamics of the nitroxide-enhanced

Published OnlineFirst March 26, 2013; DOI: 10.1158/1078-0432.CCR-12-3726

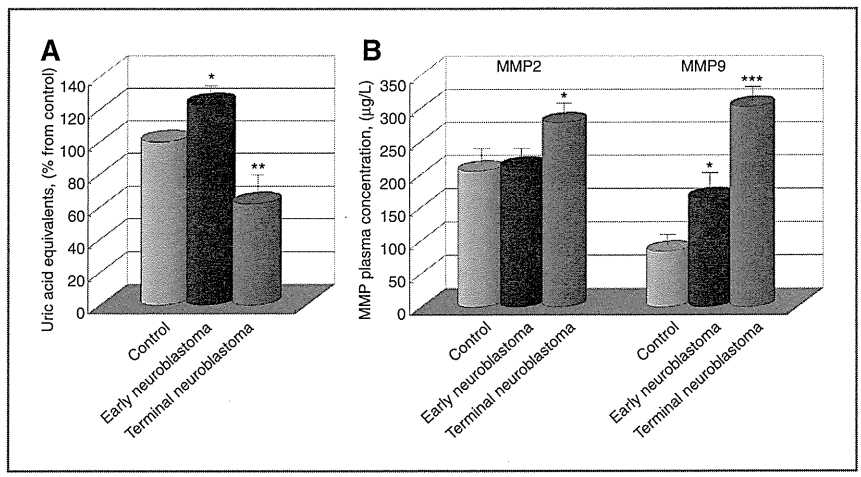

Figure 7. A, TAC of brain tissue in healthy and neuroblastoma-bearing mice. The data are the mean ± SD from 4 animals for each group. In the control group, TAC was considered 100%, which corresponded to 12 μmol/L uric acid equivalents per mg protein (~26 μmol/L copper reducing equivalents per mg protein). B, plasma levels of MMPs (MMP2 and MMP9) in healthy and neuroblastoma-bearing mice. The data are the mean ± SD from 4 animals for each group; *, $P < 0.05$; **, $P < 0.01$; ***, $P < 0.001$.

MRI signal in cancer-bearing mice injected with TEMPOL (partially water soluble, BBB-penetrating, and cell-penetrating), carbamoyl-PROXYL (water soluble, partially BBB-penetrating, and partially cell-penetrating), or carboxy-PROXYL (water soluble, BBB nonpenetrating, and cell nonpenetrating). The tumor was grafted in the right hind paw of C3H mice, and the left hind paw was used for comparison. The authors found that the intensity of the nitroxide-enhanced MRI/EPR signal in the noncancerous hind paw was significantly smaller than that in the cancer-bearing hind paw (22), which is similar to our observations (Fig. 3A). The authors do not provide data about the MRI/EPR signal decay in healthy mice. They have calculated that the rate of the MRI signal decay of TEMPOL and carbamoyl-PROXYL in cancerous tissue is more rapid than in noncancerous tissue of cancer-bearing mice. However, the ROI covers the central portion of the tumor (tumor core; ref. 22). It is very difficult for water-soluble and even partially hydrophobic substances to penetrate the tumor core, especially within a short time (within 15–20 minutes) and without a specific transport mechanism. In our studies, we observed a significant difference in the intensity and duration of the nitroxide-enhanced MRI signal between the tumor core and periphery in the terminal stage of cancer (data are not shown). In the tumor core, the signal enhancement was usually negligible even after the injection of cell-penetrating nitroxide (e.g., TEMPOL or SLENU). It is unclear whether the absence of a signal was a result of the rapid reduction of nitroxide or an inability to penetrate the tumor core. In this study, our ROI covers the entire cancer area, which minimizes the effect of different penetration and distribution of nitroxide in different parts of tumor (Figs. 2–5).

Most likely, for water-soluble nitroxides (such as carbamoyl-PROXYL and carboxy-PROXYL), the tumor is visualized predominantly on the basis of angiogenesis and the prolonged circulation of nitroxides in the bloodstream and/or prolonged retention in the EES of cancerous tissue. In this case, the MRI signal decay should be a result of nitroxide reduction in the bloodstream and/or EES and clearance from the organism through the kidneys. The same authors have shown that nitroxide-enhanced MRI signal appears first in kidney and after that in cancer area after injection of carboxy-PROXYL (23). Our previous report indicates that the penetration of nitroxide in cells and tissues is obligatory for MRI of the cancer based on the TRA (20).

Even when the BBB is disrupted (as in brain cancer), the water-soluble nitroxides are accumulated and retained in the EES despite penetrating the cells. This is a major contrast mechanism for the visualization of tumors using water-soluble gadolinium contrast agents.

In our study, we used SLENU, which is a strongly hydrophobic drug [octanol/PBS partition coefficient (log $P_{Oct/PBS}$) was 1.000 vs. 0.575 for TEMPOL, −0.158 for carbamoyl-PROXYL, and −2.000 for carboxy-PROXYL]. Nitrosoureas are well-known DNA-annealing agents, penetrating cellular and even nuclear membranes (35, 40). Thus, the dynamics of the nitroxide-enhanced MRI signal using SLENU (Figs. 2–5) could be attributed to its penetration into the cells and subsequent intracellular reduction/oxidation.

Recently, Davis and colleagues have reported that the dynamic of nitroxide-enhanced MRI is very heterogeneous in different tissues of the same cancer-bearing organism (24). We also established that the intensity, half-life, and duration of nitroxide enhancement were different in brain tissue, tissues around the brain, and muscle tissue of the hind paw (Figs. 3–5; refs. 21, 39). Moreover, different cancerous tissues (e.g., glioma and neuroblastoma) showed heterogeneous dynamic of nitroxide-enhanced MRI (Fig. 3A vs. 5B). Heterogeneity of the signal existed in the same cancerous tissue using different cell-penetrating nitroxide probes: SLENU or TEMPOL (Figs. 5 and 6). Therefore, the different rates of MRI signal decay could be a result of overlaping of several processes occuring simultaneously in tissues: different penetration rates, different reduction rates, different retention time, and different excretion rates of nitroxide from different tissues.

Published OnlineFirst March 26, 2013; DOI: 10.1158/1078-0432.CCR-12-3726

The different interpretations of the experimental data from the nitroxide-enhanced MRI studies that are published in the literature can be explained by several reasons: (i) the use of nitroxides with different cell-penetrating ability, place of retention, and excretion rate, (ii) the heterogeneity of the signal in different tissues (as a result of their different structure and metabolism), (iii) the heterogeneity of the signal in same tissue for different cell-penetrating nitroxide probes (as a result of their different pharmacokinetics), and (iv) the different analytic approaches (conclusions based on: rate of MRI signal decay, half-life of nitroxide-enhanced MRI signal, and intensity of nitroxide-enhanced MRI signal; refs. 19–24).

Each of the previous interpretations is correct, but none of them takes into account all factors that may affect the intensity and dynamics of nitroxide-enhanced MRI signal in living organism. To assess whether oxidation dominates over reduction in carcinogenesis or vice versa, it is necessary to compare the intensity and dynamics of nitroxide-enhanced MRI signal (rate of decay or half-life) in the same tissue between 2 animal species—healthy and cancer bearing. Only in this case, the penetration, retention, and excretion of nitroxide will occur at approximately same speed in the selected ROI, allowing us to ignore the impact of these factors on the dynamics of the signal. Because the cancerous tissue is completely different (structurally and metabolically) from noncancerous, presumably, the most indicative parameter for its redox activity is the duration of nitroxide-enhanced MRI signal. The presence of long-lived signal in the cancerous tissue, whereas in healthy tissues it is on baseline (Fig. 8), is an indicator for the presence of nitroxide in oxidized form, respectively, for the higher tissue-oxidative activity in cancer. The results with reduced TEMPOL support this assumption (Fig. 6). In the case of reduced TEMPOL, the nitroxide-enhanced MRI signal can appear only if noncontrast hydroxylamine is oxidized to contrast-enhancing nitroxide radical. The data showed that nitroxide enhancement appeared only in neuroblastoma-bearing brain in terminal stage, but not in healthy brain or neuroblastoma-bearing brain in early stage of cancer.

Our study also shows that the tissue redox balance is very sensitive to the progression of cancer and can be used as a diagnostic marker of carcinogenesis. In the early stage of cancer, the target tissue is characterized by a high-reducing activity, whereas it is characterized by a high-oxidative activity in the terminal stage. Carcinogenesis correlates with the redox potential of nontarget surrounding tissues and tissues distant from the tumor. In both stages of cancer development, the oxidative status of noncancerous tissues increases and they become susceptible to oxidative stress and damage.

What is the potential molecular mechanism(s) of these observations? Our hypothesis assumes that the inoculation of cancer cells in the brain can be considered an "inflammatory signal" (Fig. 9; refs. 41, 42). This inoculation leads to a local migration and an activation of a wide variety of immune cells in the target tissue, especially in the microenvironment of the primary tumor locus. This activation may trigger redox imbalance due to the "oxidative burst" of the immune cells and the production and release of ROS/RNS in the grafted area. In turn, this process will activate the antioxidant defense systems in the "inflamed" area as a compensatory mechanism to prevent oxidative stress in the microenvironment of the primary tumor locus (1, 41, 42). Our study shows that the TAC of the cancer-grafted brain slightly increased in the early stage of cancer development (Fig. 7A). Because the experiments were carried out on immunodeficient mice (Balb/c nude), the early phase was comparatively short (within 3–4 or 7–9 days for brain neuroblastoma or glioma, respectively). Shortly after inoculation, cell proliferation accelerated after overcoming the immune response, and the solid tumor grew.

The initial redox imbalance and subsequent signal transduction in the grafted area could be a critical regulator of cancer progression. ROS/RNS, produced by the immune cells in the primary tumor locus, could provoke signal transduction in 3 targets with equal probability: (i) the grafted cancer cells, (ii) the surrounding normal cells, and (iii) the surrounding extracellular matrix.

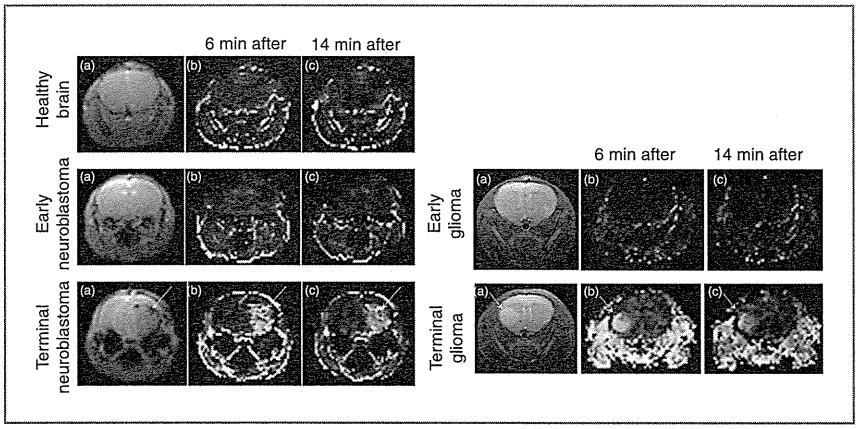

Figure 8. Typical nitroxide-enhanced MR images of healthy and cancer-bearing mice in the early or terminal stage of cancer (brain neuroblastoma or brain glioma). A, MR images of the brain with arrows indicating the tumor. B and C, extracted nitroxide-enhanced MRI signal obtained 6 and 14 minutes after injection of SLENU.

Published OnlineFirst March 26, 2013; DOI: 10.1158/1078-0432.CCR-12-3726

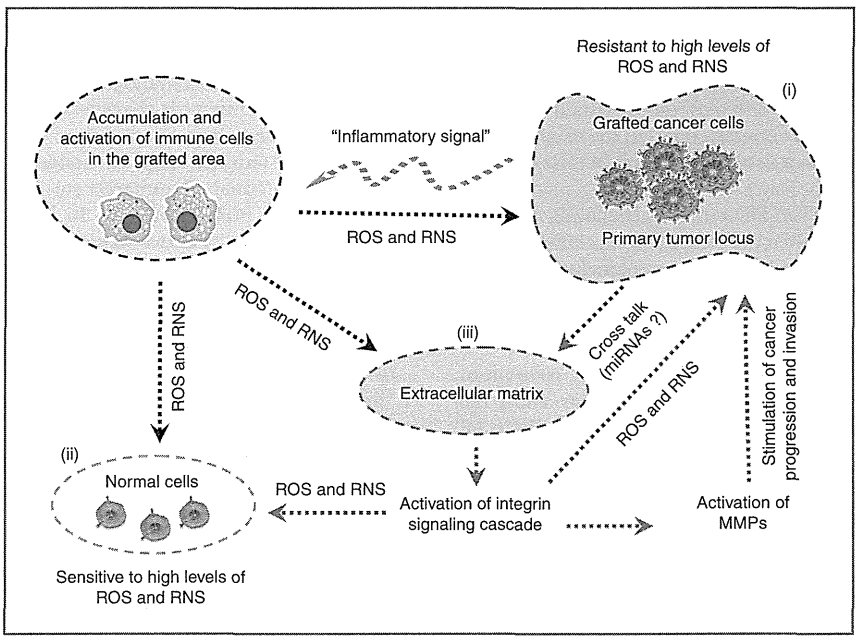

Figure 9. Molecular hypothesis. The inoculation of cancer cells in the brain can be considered an "inflammatory signal." The inoculation leads to a local migration and an activation of immune cells in the microenvironment of the primary tumor locus. ROS/RNS, produced by the activated immune cells in the grafted area, could provoke signal transduction in 3 targets with equal probability: (i) grafted cancer cells, (ii) surrounding normal cells, and (iii) the surrounding extracellular matrix. ROS/RNS and cross talk between cancer cells and the extracellular matrix activate the integrin signaling cascade. The oncogenic miRNAs, secreted by cancer cells into the environment, are considered a primary mediator of this process. The activation of integrins is linked to additional ROS/RNS production, leading to a vicious cycle. As a result, the tissue redox balance shifts toward oxidation. Cancer cells are adapted to high levels of ROS/RNS and survive. However, the normal surrounding cells and extracellular matrix are not adapted to this abnormal free radical attack and can undergo irreversible changes.

ROS/RNS have emerged as important mediators of signal transduction that are associated with the activation of the integrin pathway and modulation of integrin function through conformational changes (43). The cross talk between cancer cells and the extracellular matrix also activates integrin-related signal cascades. The oncogenic miRNAs, secreted by cancer cells into the environment, are considered a primary mediator of this process (44, 45). The activation of integrins is linked to additional ROS/RNS production by NADPH oxidases, lipoxygenases, mitochondria, etc., leading to a vicious cycle (46). As a result, the antioxidant defense system crashes with the progression of cancer and tissue redox balance shifts toward oxidation in the intermediate/terminal stage (Fig. 7A).

Integrin signaling also facilitates cell proliferation and migration, which is intimately linked to the degradation of the extracellular matrix, and activated MMPs are a prerequisite for cancer cell invasion (46). We established that the plasma level of MMP9 increases approximately 2 times even in the early stage of cancer development and approximately 3.5 times in the terminal stage (Fig. 7B). The plasma level of MMP2 also increases significantly in the terminal stage of cancer.

Cancer cells are adapted to the high levels of ROS/RNS and survive. However, the normal surrounding cells and extracellular matrix are not adapted to the abnormal free radical attack and can undergo irreversible changes. Our study also indicates that an antioxidant deficiency develops in tissues distant from the cancer locus of a cancer-bearing organism in the terminal stage. These normal tissues become highly sensitive to oxidative damage.

The data suggest that the cancerous and noncancerous tissues of a cancer-bearing organism are equally important therapeutic targets. Combining anticancer therapy with the protection of noncancerous tissues against oxidative stress may be essential for the survival and recovery of the organism.

Disclosure of Potential Conflicts of Interest

No potential conflicts of interest were disclosed.

Authors' Contributions

Conception and design: R. Bakalova, Z. Zhelev
Development of methodology: R. Bakalova, Z. Zhelev
Acquisition of data (provided animals, acquired and managed patients, provided facilities, etc.): R. Bakalova, I. Aoki
Analysis and interpretation of data (e.g., statistical analysis, biostatistics, computational analysis): R. Bakalova, Z. Zhelev, I. Aoki
Writing, review, and/or revision of the manuscript: R. Bakalova, Z. Zhelev, T. Saga
Administrative, technical, or material support (i.e., reporting or organizing data, constructing databases): I. Aoki
Study supervision: T. Saga